

the air is assumed for such a separated flow.

Table 5.7: Distribution function study results of average NPGD, NWLD, average NVD, average NKED, average liquid mass flow out of air outlet and the line average Sauter mean diameter at $x=3.5\text{ m}$; Column minimum value coloured in green and maximum in red; Fabre channel run reference 400 data (table 5.1)

Case	NPGD —	NWLD —	NVD —	NKED —	MF Liq kg/s	ave SMD mm
F_000	0.3351	0.1858	0.1791	0.5576	1.78e-04	0.2485
FDF_010	0.5255	0.1004	0.2389	0.7762	5.30e-12	13.2800
FDF_020	0.5431	0.1159	0.2719	0.7896	4.71e-11	118.9740
FDF_030	0.5597	0.1173	0.2764	0.7930	9.00e-12	19.8838
FDF_040	0.7012	0.0179	0.1742	0.5687	8.72e-11	2.3503
FDF_050	0.4497	0.0677	0.1343	0.4669	8.25e-09	0.6791
FDF_060	0.2922	0.0921	0.1410	0.4567	2.37e-08	0.4466
FDF_070	0.5616	0.0620	0.1328	0.4989	2.68e-09	0.6330
FDF_080	0.7879	0.0098	0.1501	0.4090	2.52e-09	1.1450
FDF_090	0.7201	0.2201	0.1708	0.7900	4.87e-06	0.2057
FDF_100	0.1364	0.0737	0.1322	0.5009	4.74e-10	1.9030
FDF_110	0.9022	0.0603	0.2057	0.5109	6.00e-08	0.7393
FDF_120	0.2987	0.1972	0.1713	0.5837	5.28e-06	0.6040
FDF_130	0.2884	0.1317	0.1401	0.4846	5.23e-10	0.3286

In table 5.7 the results for the distribution function comparison are shown. To emphasise good values in, they are coloured in green and bad values in red. In figure 5.8 the simulation results from table 5.7 are plotted in a chart.

Considering the figure 5.8, the smallest error overall (lowest bar height) regarding the Fabre run reference 400 data (table 5.1) has produced in simulation case FDF_100. But the physical behaviour of a multiphase flow is more complicated than choosing only the case with the smallest error. Especially the force balance between the phases determine the flow pattern, the velocity fields, as well as the pressure field. Hence the NWLD parameter has a special significance. If the NWLD is small, the simulated phase interface height is equal the interface height from the experiment. That indicates, that drag and non-drag forces nearby the interface in the simulation are approximately

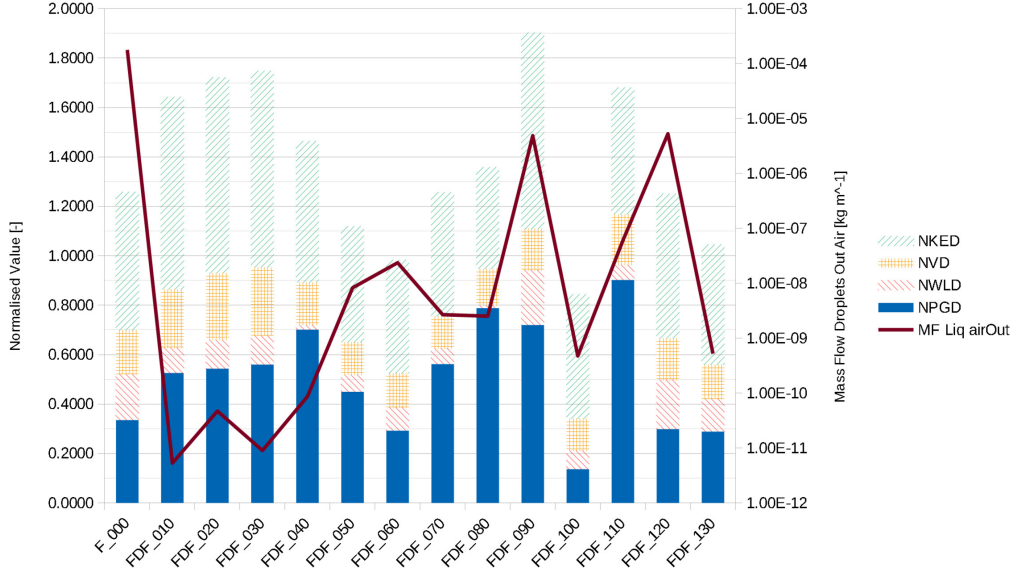


Figure 5.8: Fabre channel run reference 400 data (table 5.1) distribution function study; sum of normalised RMS kinetic energy, normalised RMS velocity, normalised water level and normalised RMS pressure gradient value for different simulation setups; figure by the author

similar to the values from the experiment. Regarding the NWLD minimum, the simulation case FDF_080 is the best. It seems that, when the force balance nearby the interface is close to the experiment, the simulated turbulence kinetic energy is close to the experiment too, see table 5.7.

The air/water separation is strongest in simulation case FDF_010, which correspond to the equilibrium distribution function. That is because of the large SMD. The same behaviour can be seen for cases FDF_020 and FDF_030 too, if one consider the average SMD and the liquid (droplet) mass flow at the air outlet. It is a plausible solution, because larger droplets have a larger inertia than smaller droplets and the air can carry rather more smaller droplets away to the air outlet.

Because of two minimum error values in table 5.7 and the overall minimum error presented in figure 5.8, the case FDF_100 is preferred.

5.4 Validation with Horizontal Channel Experiment

This validation based on the Fabre, Masbernat, and Suzanne (1987) run reference 400 data (table 5.1) experiment data, see table 5.1. As in the distribution function study a tetrahedral mesh size of 3.5 mm is used to ensure a good balance between computational effort and accuracy. In this study the simulation setup as described in section 5.1 is used, except the advection scheme. Due to better comparability an advection scheme with a constant blend factor is used. A constant blend factor of 0.75 is used. The blend factor of 0.75 means, that the first order advection is weighted with 25 % and the second order advection is weighted with 75 %. A complete second order advection solution was in some cases unstable. For comparability the reference simulation case in section 5.3 is included in this study.

In equation 3.57 a local time derivative is included. This time derivative is only available in transient simulations. Hence a transient U-RANS simulation is carried out to analyse the impact of the transient behaviour with the local time derivative in contrast to a steady state simulation. Here it should be examined whether it is possible to get steady state simulation values close to the experiment values, with a steady state simulation for a slightly transient simulation case.

Briefly a turbulence model impact is examined with a very large eddy simulation (VLES) and with a steady state BSL model simulation. It is assumed that the VLES give a better approximation of the velocity and pressure fields than a two equation model, whereby the BSL turbulence model simulation should be in between the VLES and two equation turbulence model simulation.

Due to different values for the high turbulence damping coefficient (HTC) in the literature, both values are tested.

The Sato advanced turbulence model is included in CFX as a Beta feature. Hence the behaviour of that turbulence transfer model will be tested.

Because of the completely unknown behaviour of non-drag forces in a steady state simulation, a simulation without non-drag forces is carried out. Here the impact on non-drag forces on the simulation result as well as the stability is of interest.

To determine the simulation results differences of a second order and 0.75 times second order simulation, a simulation with forced second order discretisation is carried out.

The AIAD model from HZDR is state of the art and tested well, though the blend coefficient is considered as a fitting parameter and it will be examined too.

Regarding the physical representation of a interface region, see figure 2.16, the question has been raised, whether it is not possible to leave out the free surface drag and IAD calculation and blend the droplet and bubble model with the corresponding volume fraction in this region. Hence one simulation is carried out with a blending procedure inside the free surface region between the droplet and the bubble model.

All other settings are equivalent to the mesh or distribution function study simulations.

Additional some simulation are carried out with different combination with the best particle distribution from section 5.3 and the above described parameters. These simulations have the aim, to find the best setup with the lowest error for this simulation case.

All validation simulation cases can be found in table 5.8.

The result values of normalised RMS pressure gradient deviation (NPGD), of normalised water level deviation (NWLD), of normalised RMS velocity deviation (NVD), of normalised RMS kinetic energy deviation (NKED) and of mass flow of liquid out of air outlet for all simulation cases in table 5.8, can be seen in table 5.9 and figure 5.9.

The analyses is comparable to the distribution function comparison and details can be seen in section 5.3.

Table 5.8: Fabre channel validation simulation cases overview

Case	Reference modification
F_000	Reference
FV_010	Sato advanced turbulence off
FV_020	7 equations BSL turbulence model
FV_030	blend droplet and bubble model in free surface region with volume fraction
FV_040	HTC 10
FV_050	HTC 100
FV_060	transient without local time derivative; Timestep=1e-3 s; 5 maximum inner iterations
FV_070	transient with local time derivative Timestep=1e-3 s; 5 maximum inner iterations
FV_080	switch off all non-drag forces
FV_090	switch off turbulence dispersion force for droplets
FV_100	VLES
FV_110	2nd order
FV_120	AIAD Blend Coeff 100
FV_130	$d'_{p,RRSB} = \sqrt{d_{p,max} d_{p,min}} 20$
FV_140	$d'_{p,RRSB} = \sqrt{d_{p,max} d_{p,min}} 20$; HTC 10
FV_150	$d'_{p,RRSB} = \sqrt{d_{p,max} d_{p,min}} 20$; HTC 10; 2nd order
FV_160	$d'_{p,RRSB} = \sqrt{d_{p,max} d_{p,min}} 20$; HTC 10; 2nd order; AIAD Blend Coeff 100
FV_170	$d'_{p,RRSB} = \sqrt{d_{p,max} d_{p,min}} 20$; $n = 40$; HTC 10; 2nd order; switch off turbulence dispersion force for droplets
FV_180	$d'_{p,RRSB} = \sqrt{d_{p,max} d_{p,min}} 20$; $n = 4$; HTC 100; 2nd order; switch off turbulence dispersion force for droplets
FV_190	$d'_{p,RRSB} = \sqrt{d_{p,max} d_{p,min}} 20$; $n = 4$; HTC 10; 2nd order; switch off turbulence dispersion force for droplets
FV_200	$d'_{p,RRSB} = \sqrt{d_{p,max} d_{p,min}} 20$; $n = 4$; HTC 5; 2nd order; switch off turbulence dispersion force for droplets
FV_210	$d'_{p,RRSB} = \sqrt{d_{p,max} d_{p,min}} 20$; $n = 4$; HTC 50; 2nd order;

All values in table 5.9 are averaged over 5000 iterations for steady state simulations or four times the gas flow-through time for transient simulations, except the NWLD value. The NWLD value is only available in CFX Post and

Table 5.9: Validation results of average NPGD, NWLD, average NVD, average NKED and average liquid mass flow out of air outlet (MF Liq); Column minimum value coloured in green and maximum in red; Fabre channel run reference 400 data (table 5.1)

Case	NPGD	NWLD	NVD	NKED	error sum	MF Liq
	—	—	—	—	—	kg/s
F_000	0.7619	0.2151	0.1672	0.7460	1.8902	4.54e-05
FV_010	0.5237	0.1195	0.1839	0.4608	1.2879	1.73e-04
FV_020	0.8315	0.2205	0.1578	1.2840	2.4938	7.03e-05
FV_030	0.7663	0.2257	0.1804	0.7263	1.8987	1.83e-04
FV_040	0.7396	0.2179	0.1651	0.7660	1.8886	3.14e-06
FV_050	0.5104	0.1858	0.1766	0.5227	1.3955	3.97e-06
FV_060	0.7099	0.2168	0.1681	0.7534	1.8482	2.08e-06
FV_070	0.8124	0.2118	0.1696	0.7506	1.9444	1.10e-04
FV_080	0.8776	0.2045	0.1575	0.8136	2.0532	2.20e-08
FV_090	0.6866	0.2131	0.1672	0.7414	1.8083	1.64e-09
FV_100	0.1451	0.0319	0.3478	-	0.5248	7.71e-07
FV_110	0.3743	0.1486	0.1703	0.5757	1.2689	1.57e-05
FV_120	0.5372	0.1193	0.1747	0.5191	1.3503	1.96e-04
FV_130	0.3133	0.0777	0.1428	0.6617	1.1955	4.76e-13
FV_140	0.2715	0.1176	0.1377	0.6602	1.1870	6.59e-11
FV_150	0.1124	0.0584	0.1240	0.5057	0.8005	1.61e-10
FV_160	0.1144	0.0582	0.1243	0.5034	0.8003	1.79e-10
FV_170	0.1193	0.0574	0.1244	0.5011	0.8022	1.38e-10
FV_180	0.1255	0.0652	0.1425	0.7393	1.0725	6.30e-10
FV_190	0.1534	0.0627	0.1262	0.4732	0.8155	1.42e-10
FV_200	0.1413	0.0568	0.1261	0.4705	0.7947	9.89e-11
FV_210	0.0025	0.0943	0.1367	0.6280	0.8615	9.92e-09

can not be plotted during the simulation run and is therefore an instantaneous value. Instantaneous values are dependent on the current solution field at the specific iteration or time. Hence the NWLD value is more inaccurate than average values.

Sato Advanced Turbulence Model

With the Sato advanced turbulence model, an increased turbulence in the continuous phase is caused, see section 2.4.3. Hence it is to be expected,

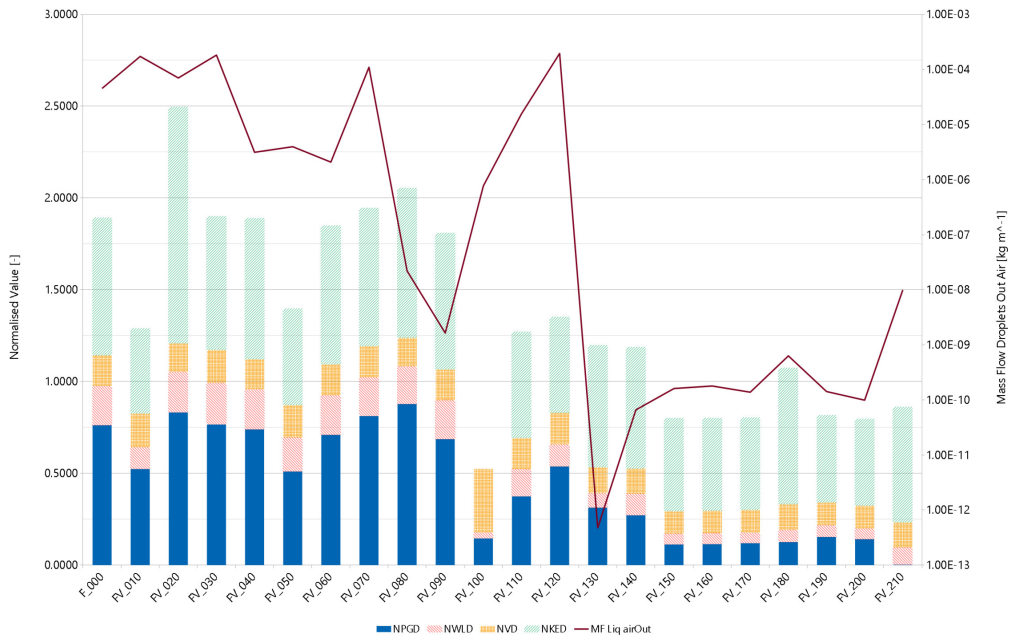


Figure 5.9: Fabre channel run reference 400 data (table 5.1) validation; sum of average normalised RMS kinetic energy, average normalised RMS velocity, normalised water level and average normalised RMS pressure gradient value for different cases; figure by the author

that the pressure drop in the gas phase is increased with this Sato model. This behaviour can be confirmed by the simulation, see in figure 5.9 the increased NPGD value of case F_000 compared to the case without the Sato turbulence transfer model FV_010. Interesting is the effect of the Sato model on the interface height. With the Sato model and thus a continuous fluid with increased kinetic energy, the water level is lower than without the Sato model. Which implies that in saturated flow regimes the turbulence of the lighter phase above the heavier phase have a strong impact of the force normal to the interface in gravity direction.

Despite of better results of the simulation case without the Sato model, the Sato model should be included in the simulation model, since without this Sato model a high droplet mass flow at the air outlet is produced. This is a result of a to high water volume fraction in the air flow above the water surface, see figure 5.10. That could an effect of droplets with high kinetic energy

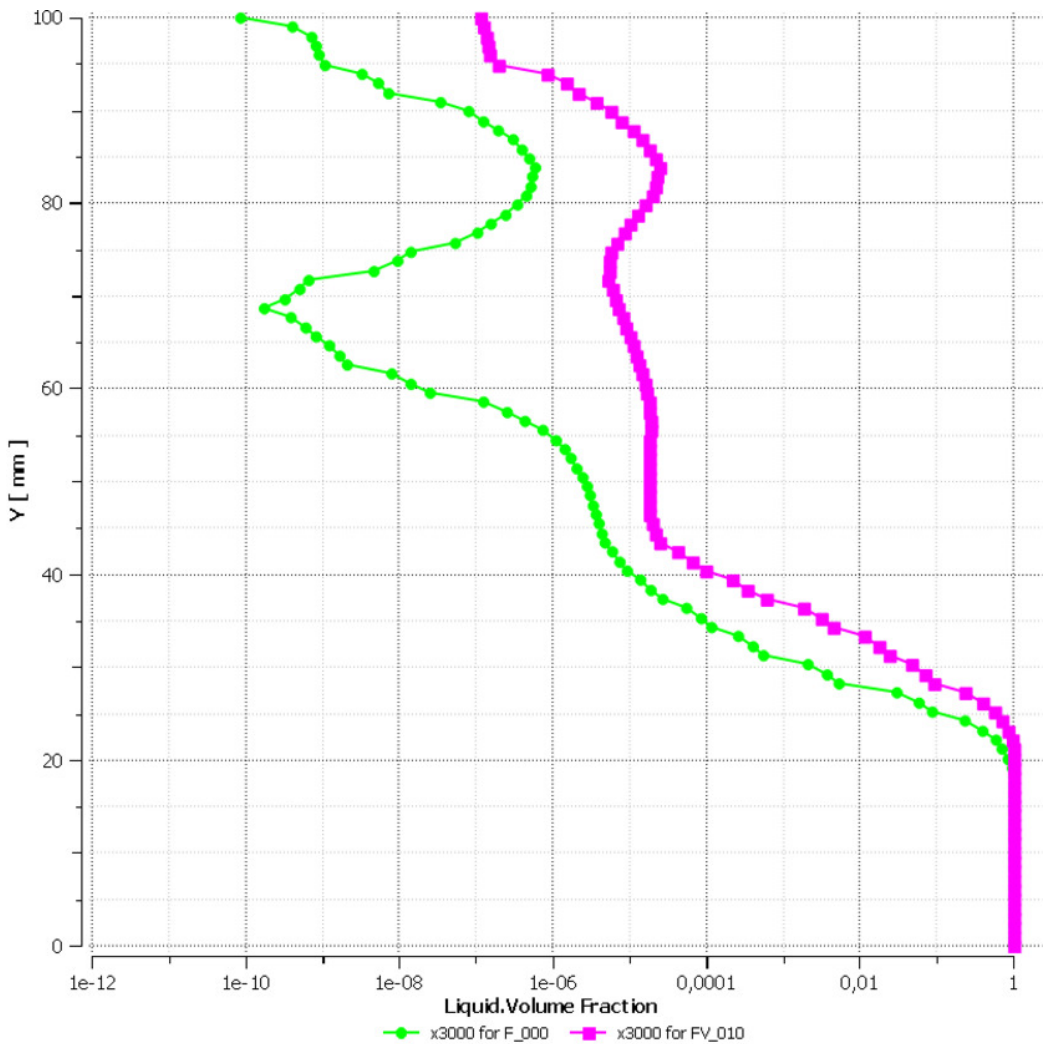


Figure 5.10: Fabre channel run reference 400 data (table 5.1) validation; Liquid volume fraction at $x = 3\text{m}$ above the channel height Y for case F_000 and FV_010; figure by the author

and so that with high droplet velocity. Droplets with high kinetic energy can be carried away better from the interface as with less kinetic energy. This yields to an increased volume fraction of water above the interface. With the Sato model, more momentum is needed of the carrier phase air to carry droplets to the air outlet than without the Sato model.

The separation of both fluids are more important for vertical flow pattern. If the separation worse, the flow pattern like slug flow or churn flow do not

occur or only at a wrong volume fraction ratio. Thus in such an intermittent vertical flow a wrong pressure drop is the result. In a horizontal saturated flow this separation is less important. The phase separation in a horizontal flow becomes only again more important for an annular flow.

Turbulence Model

The BSL Reynolds stress turbulence include the effects of "streamline curvature, sudden changes in the strain rate, secondary flows or buoyancy compared to turbulence models using the eddy-viscosity approximation" (Ansys (2016b)). Such secondary flows and free shear flow with strong anisotropy also occurs in the Fabre experiments flow pattern. But except the NVD value the BSL model have increased errors, see table 5.9. Especially the NKED value is too high in the BSL simulation, that this simulation is the worst overall. In the bubble region the kinetic energy has particularly large deviations with the BSL model, see figure 5.11.

Due to the high computational effort and the worse simulation results, the BSL Reynolds stress turbulence model is discarded and the SST turbulence model is preferred.

In general the Large Eddy Simulation (LES) should compute the turbulence more accurate and hence the SMD approximation should be better, see section 4. Hence with a LES the deviation of a steady state SST turbulence model should be figured out.

The LES is applied on a coarse RANS mesh with the wall function approach, which then called Very Large Eddy Simulation (VLES). The mesh which is used in the steady state reference case F_000 is used for the VLES case FV_100 also. Like in the other transient simulations, the Courant number is about 1.5 in the VLES too. To calculate the relative fluid acceleration, the local time derivative is included, like in case FV_070.

The momentum imbalances in case FV_100 are always between +/- 1 %, but the mass imbalances fluctuate in between -30 % and 30 %, but the average is 0. Despite of the same mesh and Courant number the convergence of the

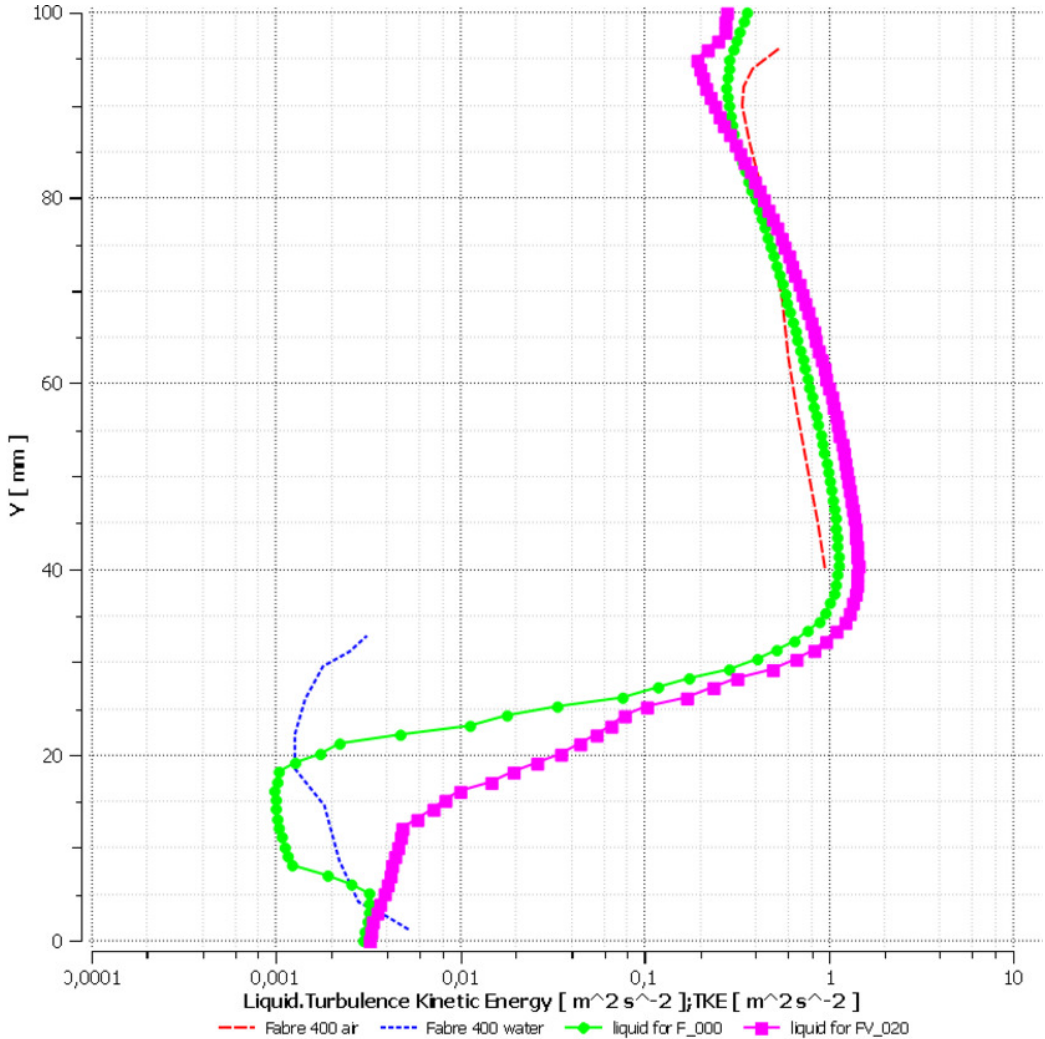


Figure 5.11: Fabre channel run reference 400 data (table 5.1) validation; Kinetic energy at $x = 3\text{m}$ above the channel height Y for case F_000 and FV_020; figure by the author

pressure field is much slower for the VLES than cases FV_060 and FV_070. The VLES simulation takes about 7.5 times of the simulation time compared to the case F_000.

In Fabre, Masbernat, and Suzanne (1987) one can see, that the Fabre reference 400 flow is wavy stratified. The case FV_100 is the only of all cases in table 5.8, which results to a wavy stratified flow pattern, with a wave length about some 1-5 cm. Whereby the others simulation are rather only a

stratified flow, with a wave length about 1 m. The waves in the VLES could be one of the reasons for the longer convergence.

In figure 5.9 it can be seen, that the VLES case FV_100 has the lowest error overall. Due to the small NWLD and NPGD value of case FV_100 it is assumed, that the forces on the interface are close to the experiment. But the VLES have the worst value for the NVD, see table 5.9. This is probably due to the coarse mesh, because the velocity deviation in the VLES case is more in the droplet region with higher velocities, see figure 5.12. In the water region the VLES simulation results are closer to the Fabre, Masbernat, and Suzanne (1987) results and better than the SST turbulence model velocities. The VLES simulation has a smaller droplet mass flow at air outlet, which reinforces the assumption, that the SST turbulence model have an increased phase diffusion.

Despite of the coarse mesh the VLES showing good results for the pressure drop and phase distribution. Also the VLES is the only simulation which shows a wavy stratified flow. But due to the multiple simulation time compared to a steady state SST simulation, it would take too much time for a large industrial application like a steam drum for the current situation. But with increasing cpu power in future, the VLES could be a good choice for larger applications too.

Free Surface Particle Model

Like mentioned above, the question has occurred, whether it is not possible to replace the drag and IAD calculation for the free surface region and blend the bubble and droplet results with the volume fraction in this region.

Except the droplet mass flow rate at air outlet, all error values are close to the Reference case. The different mass flow is caused by an increased momentum transfer at the interface. This increased momentum transfer can be seen in figure 5.13 at $y = 25$ mm. In this figure the Interface Area Density (IAD) times the drag coefficient (CD) is shown. In equation 2.52 one can see, that the interface drag is increased, if IAD*CD is increased too.

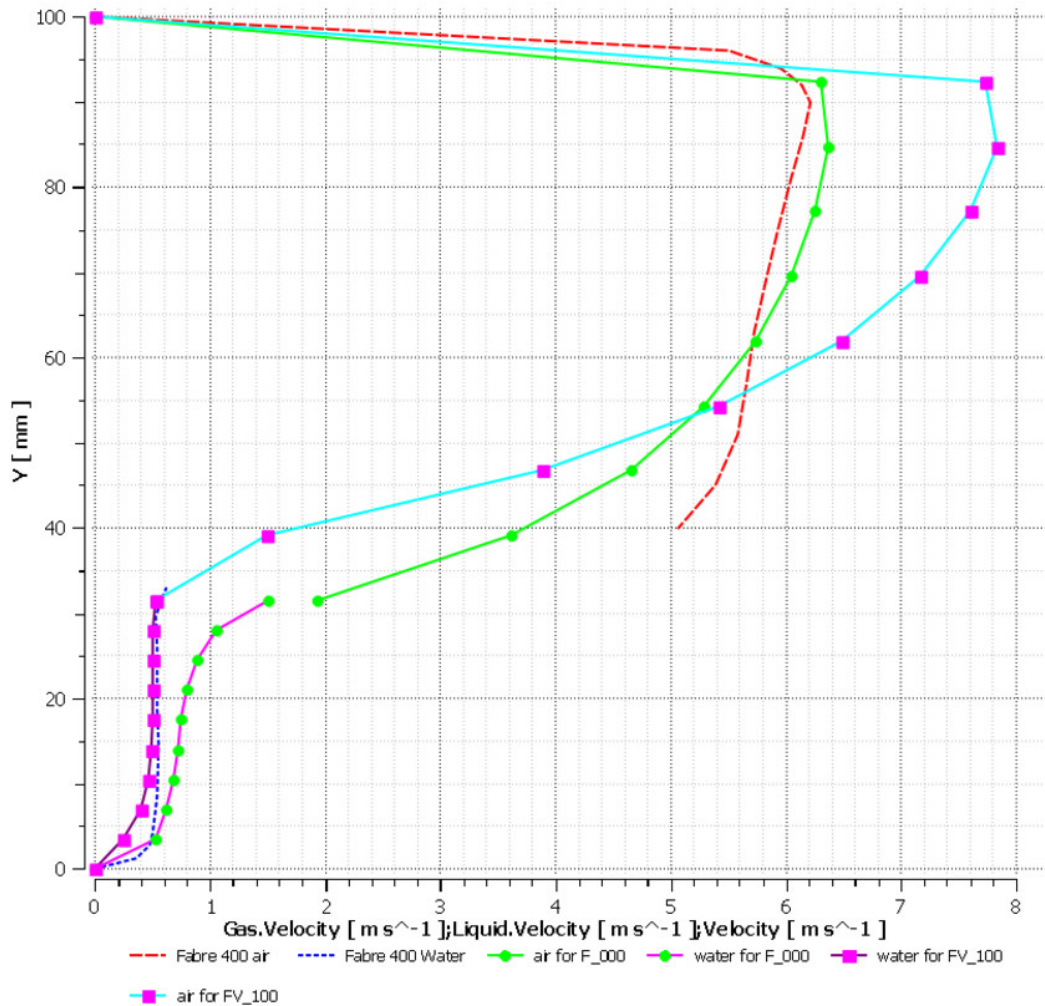


Figure 5.12: Fabre channel run reference 400 data (table 5.1) validation; Velocity at $x = 3\text{m}$ above the channel height Y for case F_000 and FV_100; figure by the author

With this increased momentum drag for case FV_030 the water is pushed stronger against the outlet wall. Therefore more water is redirected to both outlets. Thus the droplet mass flow at air outlet is higher for case FV_030.

The difference IAD and CD values in case FV_030 is a direct result of the replaced free surface model. Hence it is recommended to use the free surface model to calculate the IAD and CD values for the interface region.

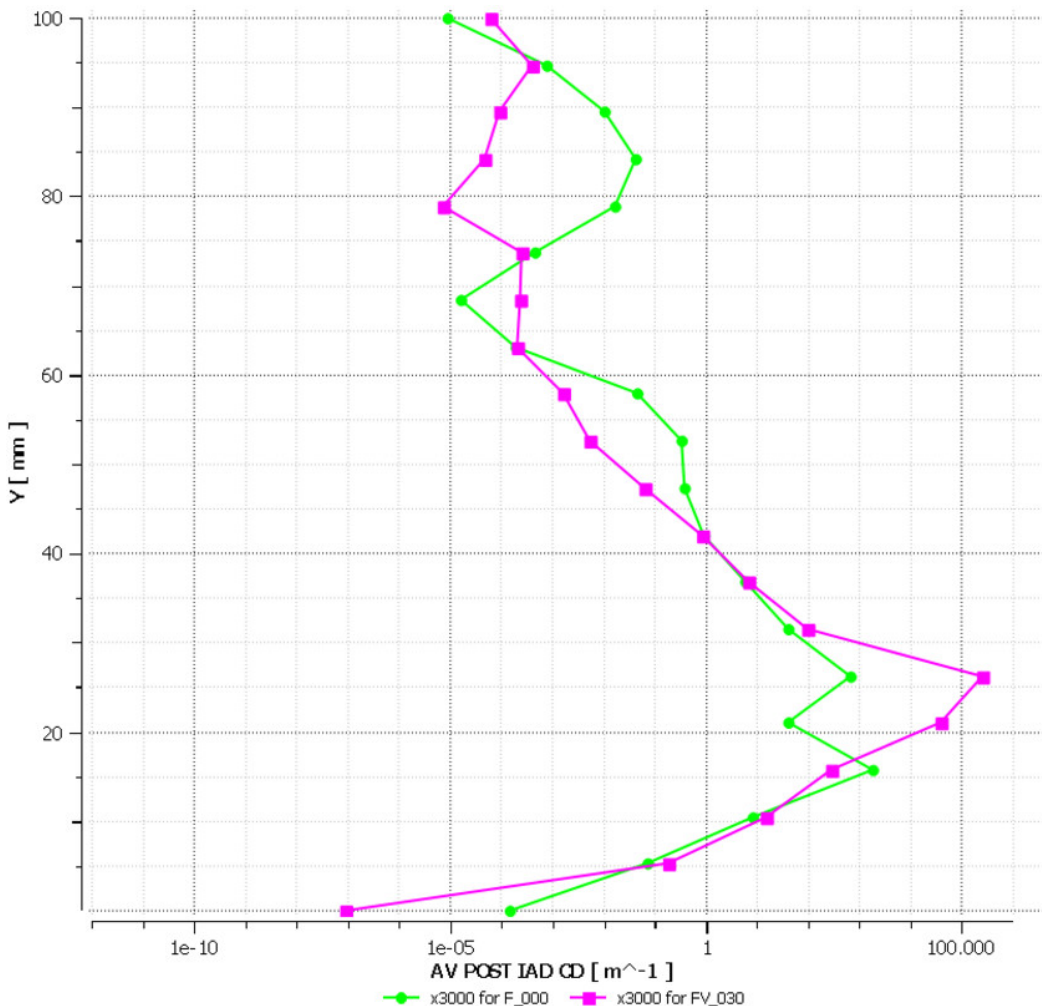


Figure 5.13: Fabre channel run reference 400 data (table 5.1) validation; IAD times CD at $x = 3\text{m}$ above the channel height Y for case F_000 and FV_030; figure by the author

High Turbulence Coefficient Examination

On the one side Porombka and Höhne (2015) recommend a High Turbulence Coefficient (HTC) of about 100. On the other side Ansys (2016d) has a default value of 10. Hence both HTC values will be tested with the Fabre experiment simulation.

The HTC value increase or decrease the turbulence damping in the free surface region, see section 2.4.3. The turbulence damping caused a increasing

ω -value of each phase. Thus the kinetic energy is decreased in this region, see figure 5.14, if the HTC value is increased.

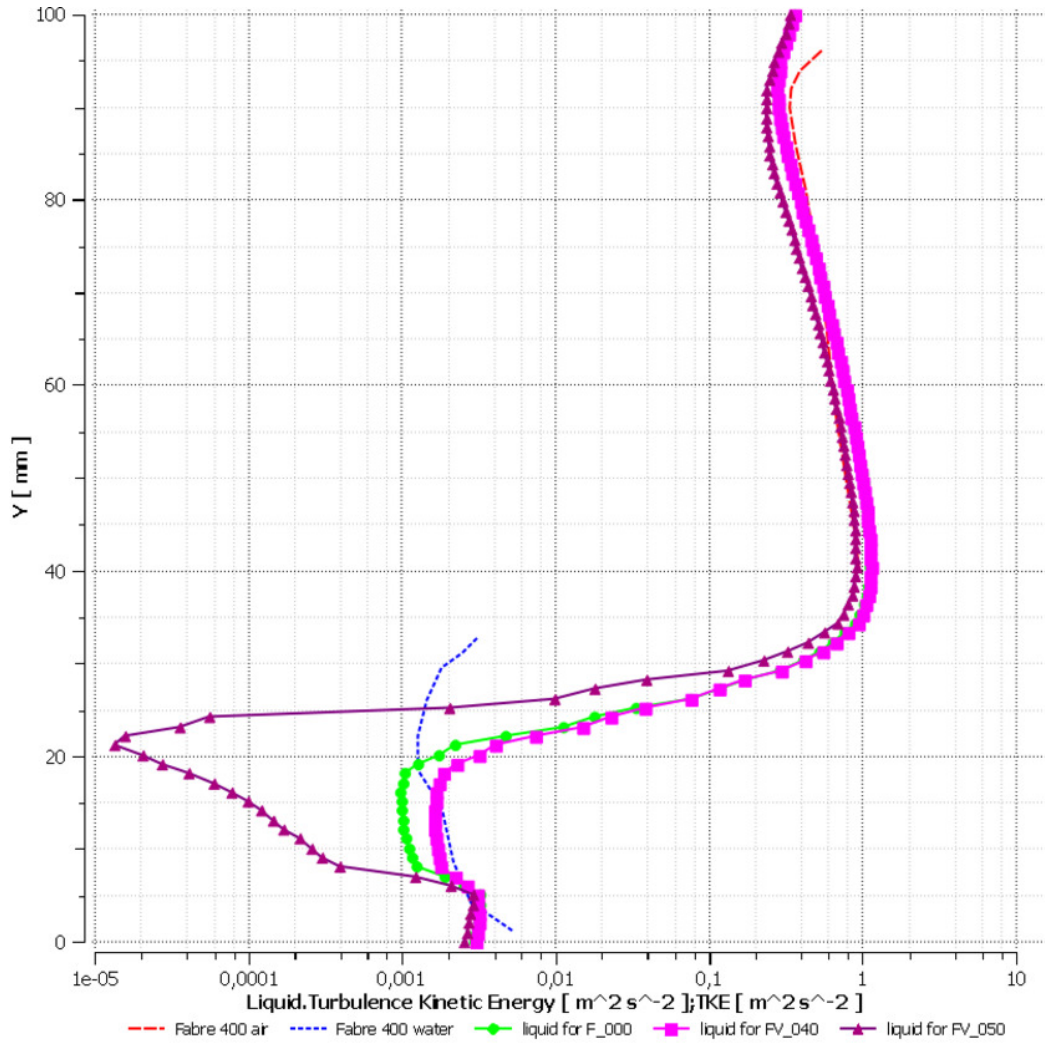


Figure 5.14: Fabre channel run reference 400 data (table 5.1) validation; Kinetic energy at $x = 3\text{m}$ above the channel height Y for case F_000, FV_040 and FV_050; figure by the author

Despite of the large visual deviation of the kinetic energy regarding the case FV_050, this case has the low NKED value. Also the most error values of case FV_050 are smaller than cases with lower HTC values. Thereby the overall error of case FV_050 is the smallest compared to F_000 and F_040. Hence a HTC value of 100 is recommended, but the large kinetic energy

deviation in the water phase is considered critical.

Transient Impact

In general the transient simulations are running 4 times longer than the steady state simulation. The mass and momentum imbalances are below 1%, to ensure stable simulations. The momentum imbalance condition can be satisfied with a Courant number of about 1.5 for the transient simulations, whereby the case FV_060 have much larger mass imbalances than case FV_070, at the same Courant number. In this simulation the drag coefficient depends indirect on the time derivative. This latter cause an error in Ansys CFX. In section [5.1.5](#) a solution for this CFX error is presented.

In table [5.9](#) one can see, that the transient simulations FV_060 and FV_070 are close to the reference. Especially the NVD and NKED values are close to each other. The main difference between these simulation cases is the droplet mass flow out of air outlet. The largest droplet mass flow is at case FV_070 and the smallest at case FV_060. The Reference case lies in between. This droplet mass flow behaviour can be explained with figure [5.15](#).

At Y-value = 100 mm there is the top wall of the channel. Nearby the end of this top wall there is the air outlet. If the drag force increased at the top wall, the water film at this wall is pushed away from the air. Hence the mass flow of droplets at air outlet is increased. In figure [5.15](#) one can see high drag forces for the case F_000, medium drag forces for FV_070 and the lowest drag forces for the case FV_060 nearby the top wall. This correspond to these different droplet mass flow rates in table [5.9](#).

We can assume that transient simulations are more accurate than steady state simulations, because the steady state is one special case of a transient simulation without local temporal changes. Then we can suppose that the steady state simulation over predict the drag force in the droplet region, see [5.15](#). Hence a too high droplet mass flow can be expected, see equation [2.52](#). And the steady state simulation under predict the drag force nearby the bottom wall in the bubble region, so that less bubbles are carried away nearby the bottom wall. But due to the low liquid volume fraction in the droplet

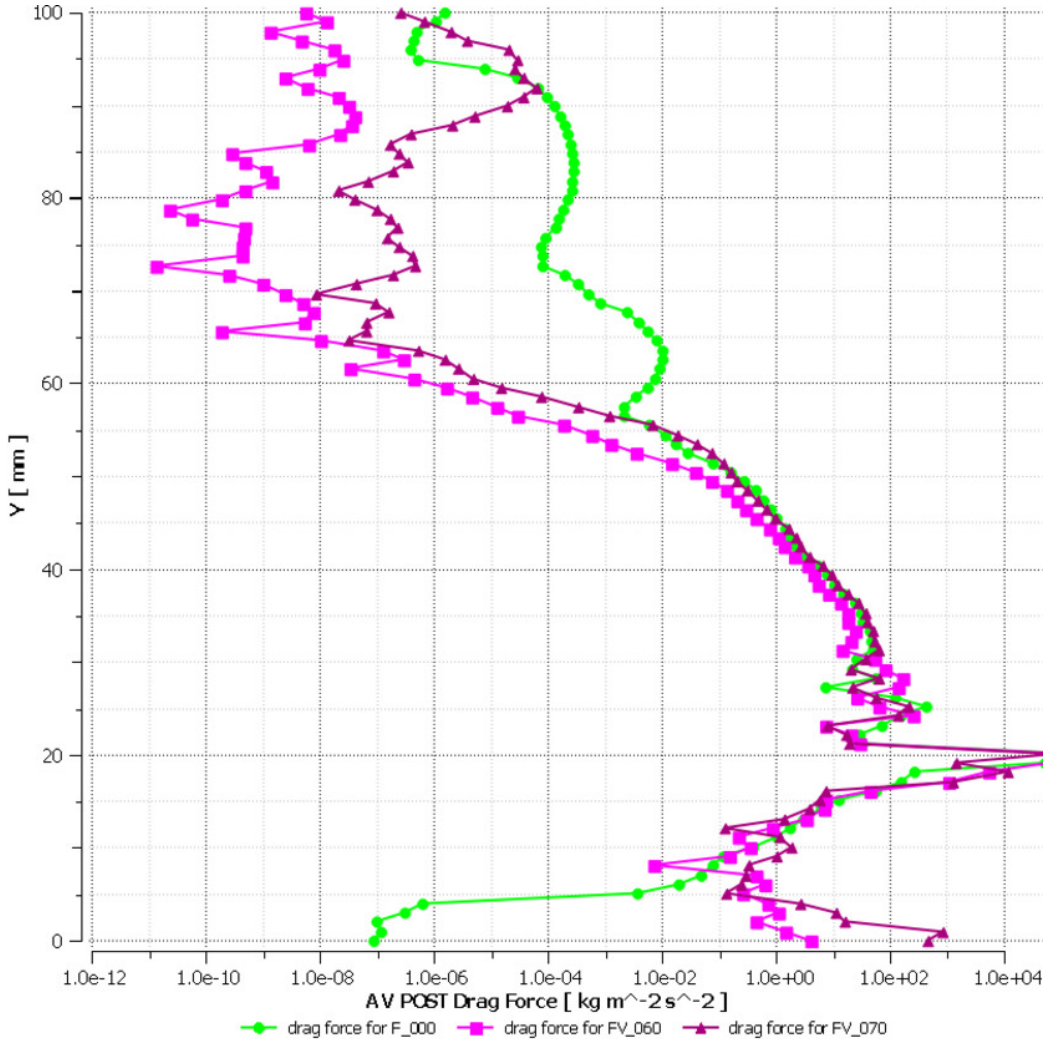


Figure 5.15: Fabre channel run reference 400 data (table 5.1) validation; Drag force at $x = 3\text{m}$ above the channel height Y for case F_000, FV_060 and FV_070; figure by the author

region and low gas volume fraction in the bubble region, the impact of these different drag force curve shapes in these simulations is small regarding the NPGD, NVD and NKED values. This over predicting drag force is caused by a too high IAD which can be seen in figure 5.16, what is again a result of too high liquid volume fractions in the droplet region, see figure 5.17. The relation between IAD and volume fraction for the particle model can be seen in equation 2.38.

Only regarding the phase distribution there are differences between the steady state and transient simulation. Hence it could be possible to correct the IAD or CD value for a steady state case, in order to achieve good results and a decreased computational time at the same time.

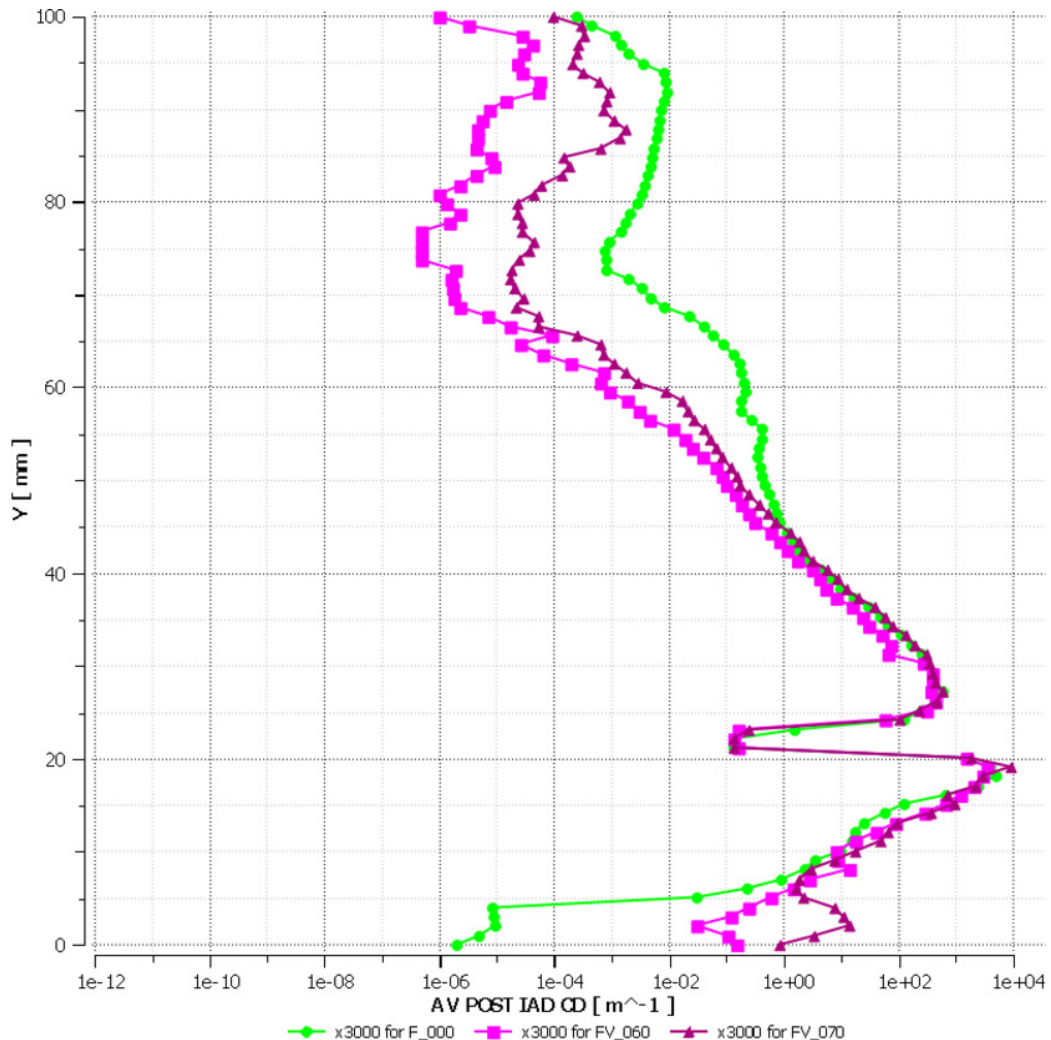


Figure 5.16: Fabre channel run reference 400 data (table 5.1) validation; Interface area density times drag coefficient at $x = 3\text{m}$ above the channel height Y for case F_000, FV_060 and FV_070; figure by the author

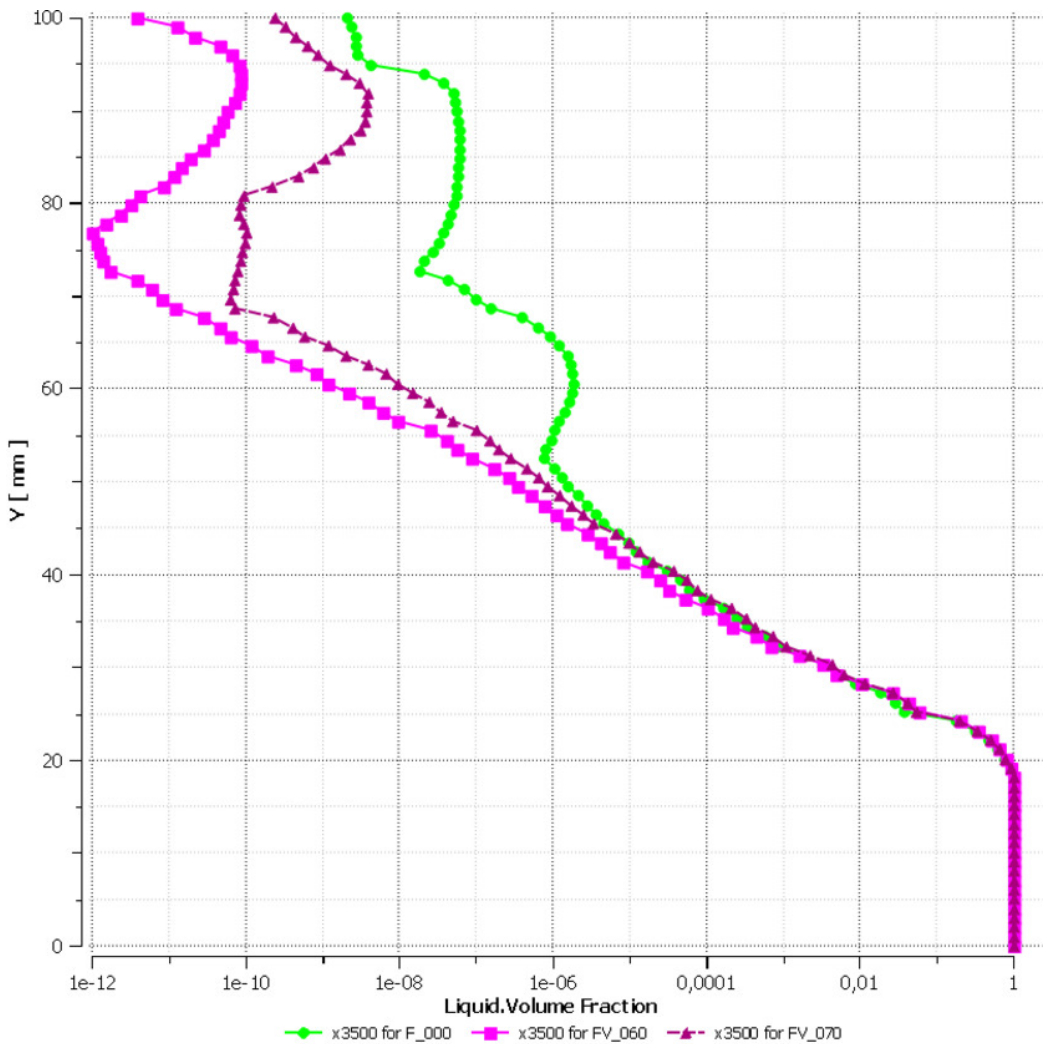


Figure 5.17: Fabre channel run reference 400 data (table 5.1) validation; Liquid volume fraction at $x = 3\text{m}$ above the channel height Y for case F_000, FV_060 and FV_070; figure by the author

Impact of Non-Drag Forces

In figure 5.9 it can be seen, that the simulation cases FV_080 and FV_090, which have different non-drag forces than the case F_000, the overall error do not differ so much. The evident difference is the droplet mass flow out of air outlet.

Consequential the non-drag forces increase the droplet transport transverse

to the flow direction. The turbulent dispersion force causes particles from regions of high concentration to low concentration, see section 2.5.3. Hence this force cause mainly a high droplet mass flow at air outlet. In figure 5.9 it can be seen, that the droplet mass flow at air outlet is significantly decreased, if the turbulent dispersion force is switched off for the droplets.

Second Order Advection Scheme

In general the error decrease faster for a second order advection scheme than a first order for more and more smaller cell sizes. So it is recommended to use the second order scheme. But at some simulation model combinations the solution is unstable, why a blending factor of 0.75 between first order and second order is used. With this blending factor of 0.75 all the simulations are run stable. For the reference case F_000, it is possible to run with the second order scheme. The second order case FV_110 have a decreased error for the NPGD, the NWLD and the NKED value. Though both NVD and droplet mass flow at air outlet values are closed together. Hence the overall error of the second order scheme case is smaller than the reference case, see figure 5.9. Hence it is recommended to use the second order advection scheme if possible.

AIAD Blend Coefficient

In the literature the recommended AIAD blend coefficient is 50. But no parameter study can be found that examine this blend coefficient. In case FV_120 the AIAD blend coefficient is increased to 100. This latter has a positive effect on the NPGD, NWLD and NKED value. This is mainly an effect of the decreased drag force nearby the interface, see figure 5.18.

The NVD value is slightly worse but the droplet mass flow at air outlet is much higher. Due to the increased blend coefficient the diffusion of the droplets from the interface is stronger, so that more water is carried away by the air, see figure 5.19.

A final statement can not be made, whether it is better to use an AIAD blend coefficient of 50 or 100. Hence in the following combination of the

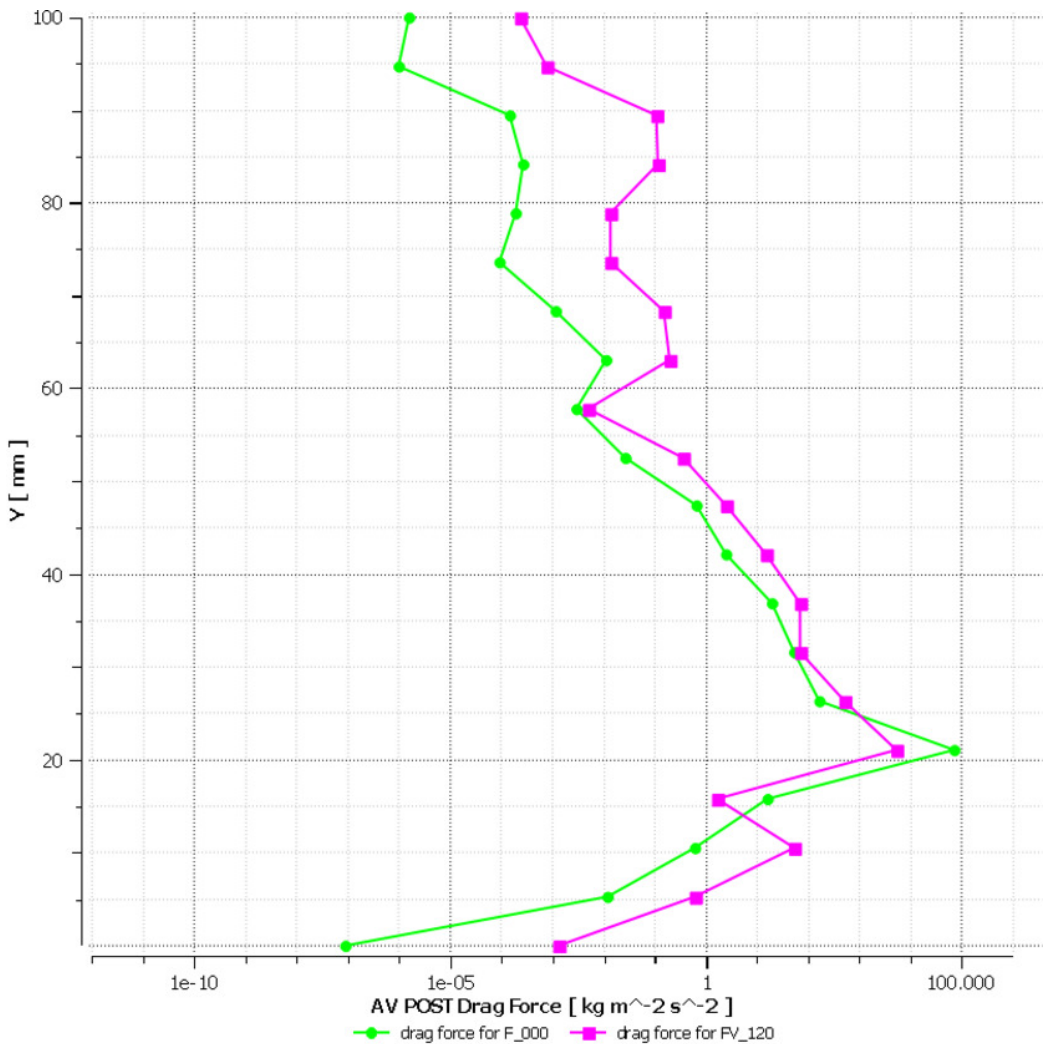


Figure 5.18: Fabre channel run reference 400 data (table 5.1) validation; Drag force at $x = 3\text{m}$ above the channel height Y for case F_000 and FV_120; figure by the author

above examined parameter this blend coefficient should be examined in more detail.

Combinations

Following simulations are combinations of the distribution function study results and first results of the validation simulations. Here it is tried to find a good combination of the distribution function, solver and model parameters,

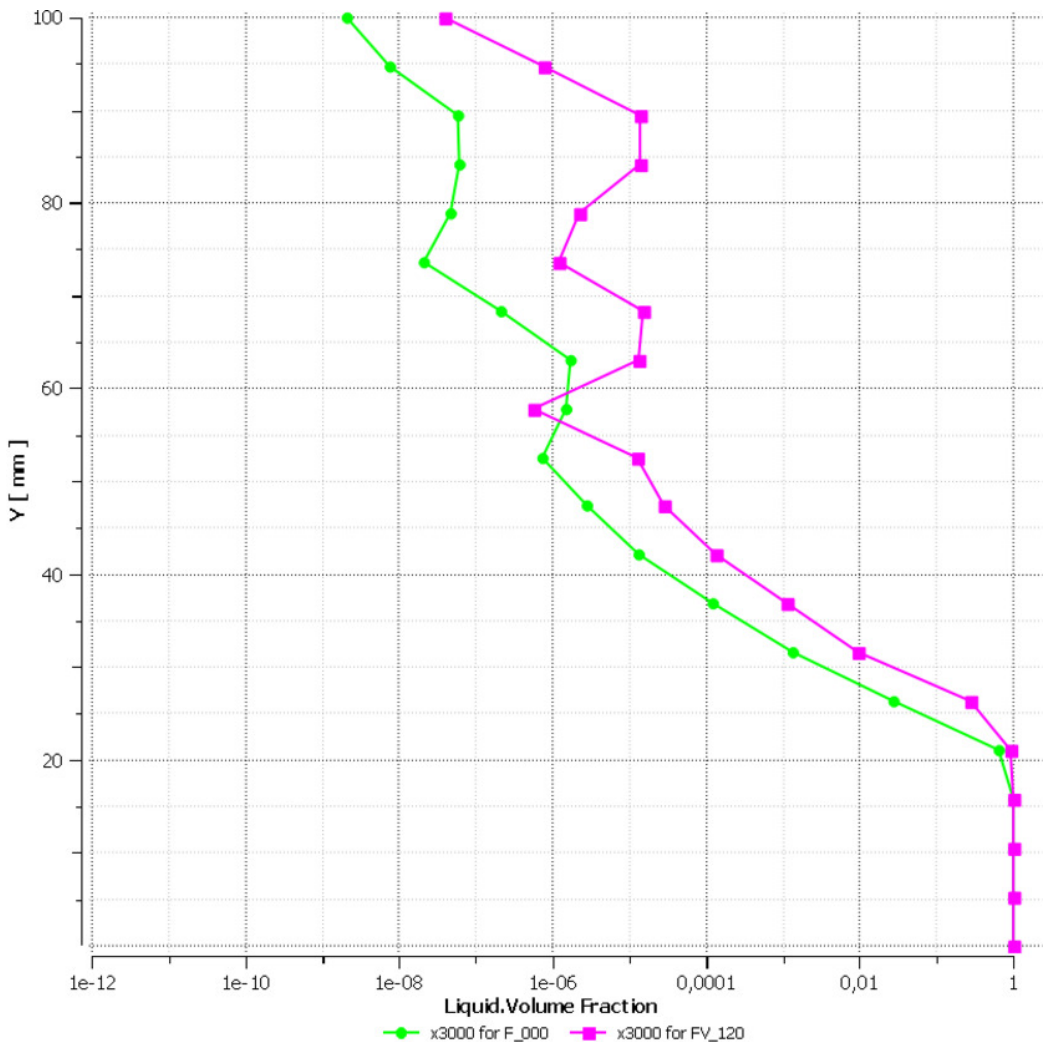


Figure 5.19: Fabre channel run reference 400 data (table 5.1) validation; Liquid volume fraction at $x = 3\text{m}$ above the channel height Y for case F_000 and FV_120; figure by the author

as well as models itself.

From the distribution function study two cases are preferred, see section 5.3. Both cases have a SMD correction factor of 20 overall, but in one of these cases a RRSB shape value of $n=40$ is used and in the other case the RRSB shape value is $n=4$. Both cases are used in the following combinations, see table 5.8.

Keep in mind, that the constant specific blend factor of 0.75 for the advection

scheme is used in the validation study, but the High Resolution model for the advection scheme in the distribution study. Hence case FV_130 and case FDF_080 differ in that point, despite otherwise equal setup.

If we consider all cases with a RRSB shape value of n=40 and a SMD geometric mean correction factor of 20, cases from FV_130 to FV_160, we can see that these cases have the strongest phase separation. This strong phase separation is caused by larger particles due to the SMD correction factor, which also can be seen in the distribution study in table 5.7. This statement applies to all cases with larger SMD values. Through additional setup modifications, this effect can be enhanced or reduced, see figure 5.9.

For example a increased HTC value should be reduced the overall error with only a slightly change in the droplet mass flow at air outlet, see paragraph [High Turbulence Coefficient Examination](#). But in case FV_140 it can be seen, that with a decreasing HTC value the simulation errors are decreasing too. Only the phase separation is worse with a decreasing HTC value, what can not be verified in paragraph [High Turbulence Coefficient Examination](#). It may be that some models counteract this decreasing HTC value effect.

There are some positive effects if a second order advection scheme is used, how is described in paragraph [Second Order Advection Scheme](#). This positive effect can be seen in case FV_150 too. Hence the overall error is decreased with a second order advection scheme. Only the mass flow of droplet at air outlet is increased.

As described in paragraph [AIAD Blend Coefficient](#), a AIAD blend factor of 100 reduce the overall error but leads to an increased droplet mass flow at air outlet. In case FV_160 an AIAD blend coefficient of 100 is used, but all differences compared to case FV_150 are go down in the numerical noise. Hence a further analysis of this blend factor is not recommended.

The significantly reduction of the droplet mass flow at air outlet without the Turbulent Dispersion Force (TDF) for the droplets can not be validated with the case FV_170. All differences of cases FV_150 and FV_170 are in the numerical noise. Hence the TDF can be calculated or not for a horizontal separated flow.

Case FV_180 to FV_210 showing the error differences, if the HTC value is changed. When one compare the overall error, it can be seen, that case FV_200 is the simulation with the lowest error, even for all cases in table 5.9.

According to table 5.9 the overall error of cases FV_150, FV_160, FV_170, FV_190 and FV_200 are close together. But case FV_200 has from the latter best cases the smallest droplet mass flow at air outlet. Hence the recommended case in this validation is FV_200.

5.5 Fabre Conclusion

In chapter 3 a new general simulation model is developed, in order to simulate a two-phase flow without the use of global parameters, like pipe diameter. This new model should be fast and robust in order to be applied to large industrial applications. In section 5.2 the impact of the mesh size to the new model is analysed. In the mesh study the normalised pressure gradient deviation (NPGD) is used to examine the mesh independency. Smaller tetrahedra sizes than 3.5 mm causes no large NPGD value deviations. But only from a tet size of 1.75 mm the NPGD error is smaller than 1% and is recommended.

With the knowledge of the mesh study, a distribution study is carried out. In section 5.3 the best performance is achieved by cases FDF_080 and FDF_100. Later cases are uses the RRSB distribution function with a Sauter mean diameter correction factor of 20.

Due to the complexity of this new simulation model additional simulation are necessary, in order to examine the behaviour of the individual submodels. For this purpose a validation is carried out in section 5.4, where first the impact of the submodels is examined. Afterwards the submodels are modified and combined to reduce the overall error. Here the error could be decreased again. The best combination of submodels is case FV_200. But the error in cases FV_150, FV_160, FV_170 and FV_190 are close to the case FV_200.

Chapter 6

Proof of Concept with Vertical Test Case

Like mentioned in the introduction in section 5, the predominant flow pattern in a steam drum is a stratified flow. But in the feeding pipes of a ERK steam drum, there are some regions with vertical flow pattern. The goal of this thesis is to develop a two-phase simulation model for industrial applications like steam drums, which is independent of the geometry. Hence the vertical flow regimes should be take into account too. Hence subsequently the simulation model was tested for horizontal flows, a proof of concept for a two-phase flow for a vertical pipe is carried out. So this new two-phase model is tested for a broader range of multiphase flow regimes.

The proof of concept test case is the Hewitt and Owen (1987) experiment. In order to compare the results from the horizontal test case, the physical set-up of validation case FV_190 is used in this chapter. For the specific values see section 5.1.3 and table 5.8. Only the different material parameter, see table 6.1, will be changed in those following simulations. The case FV_190 was preferred to case FV_200, because FV_200 yields to unstable simulations sometimes.

6.1 Hewitt Model

In [Hewitt and Owen \(1987\)](#) one can see the complete description of the vertical two-phase flow experiment. The goal of this experiment from [Hewitt and Owen \(1987\)](#) is to predict a fully developed flow in a uniform vertical pipe. The vertical pipe has a 31.8 mm inner diameter and its total length is 23 m. This long pipe ensures a development length of about 570 diameters. The scheme of the experiment set-up can be seen in figure [6.1](#).

[Hewitt and Owen \(1987\)](#) use air and water as fluids, which corresponds to the Fabre experiment fluids in section [5.1](#). In this experiment the water mass flux is constant and the air mass flux is increased. In table [6.1](#) there are the constant parameters of this experiment.

Table 6.1: Hewitt vertical pipe experiment constant parameter; [Hewitt and Owen 1987](#)

Water mass flux	297.1 kg/(m ² · s)
Water density	998.5 kg/m ³
Air density	2.9 kg/m ³
Water dynamic viscosity	0.001 Pa · s
Air dynamic viscosity	0.000018 Pa · s
Surface tension	0.0726 N/m

[Hewitt and Owen \(1987\)](#) measure the pressure gradient between the pressure taps in figure [6.1](#). Furthermore informations about the observed flow pattern is given. The air mass flux is in range of 2.96 to 161.69 kg/(m² · s), which correspond to bubble flow pattern up until annular flow pattern. The pressure gradient and observed flow for two crucial cases can be seen in table [6.2](#). This restriction to two cases can be done, because mainly bubble and slug flows could be observed in the steam drum experiment in section [7.1](#).

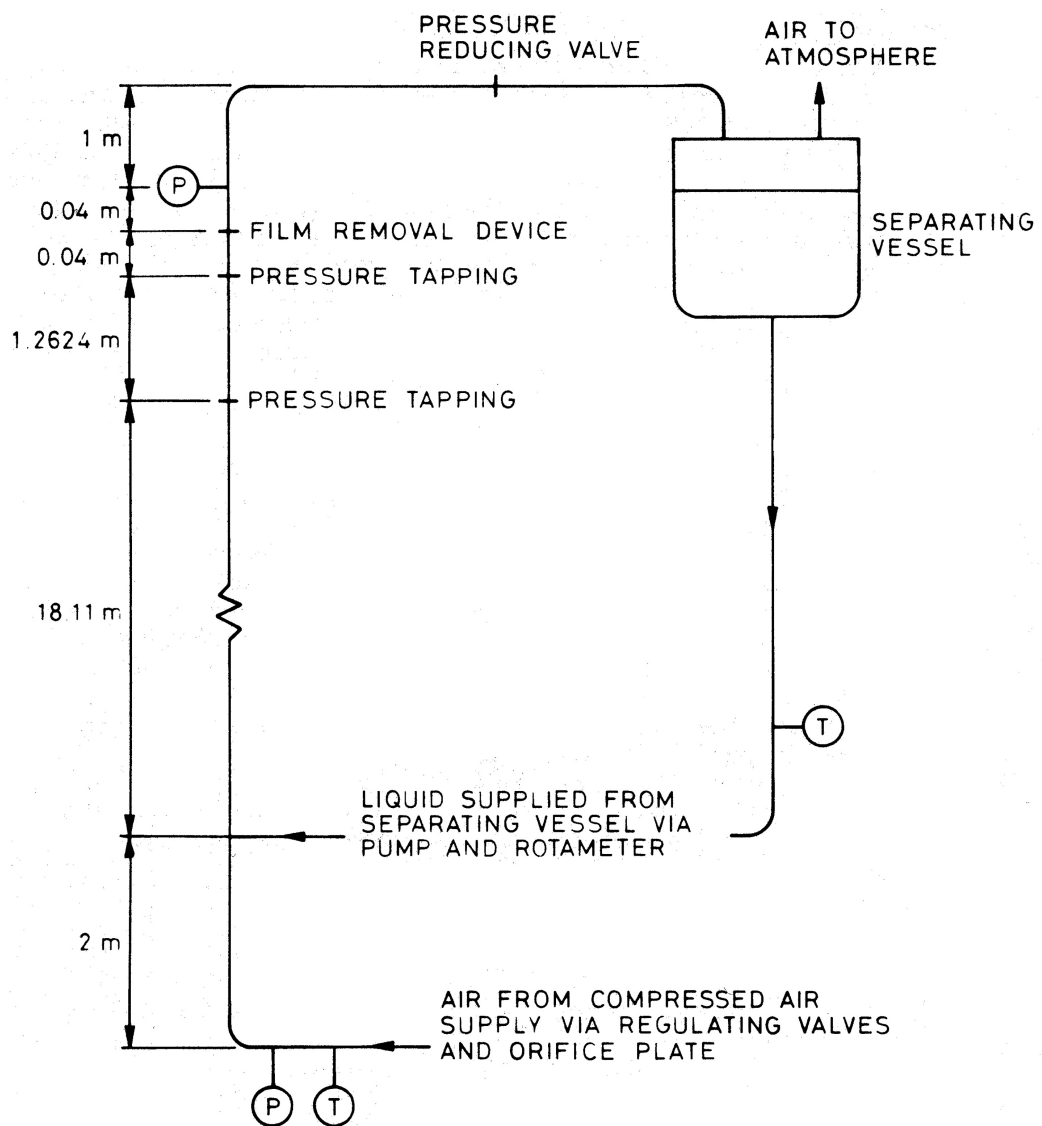


Figure 6.1: Hewitt and Owen (1987) experiment set-up scheme; see Hewitt and Owen 1987

Table 6.2: Extract of Hewitt vertical pipe experiment results; observed flow regime and pressure gradient; Hewitt and Owen 1987

Run No.	Air mass flux [kg/(m ² · s)]	Pressure gradient [Pa/m]	Observed flow regime
1	2.96	9489.0	Bubble
6	8.50	2876.0	Slug

6.1.1 Hewitt CFD Geometry and Mesh

The Hewitt and Owen (1987) experiment is about 20 m long vertical pipe with an inner diameter of 31.8 mm. In earlier examinations it was tried to reduce the computing time with a quarter and a half part of the vertical pipe compared to a full pipe. In the quarter and half part pipe simulations, the observed flow pattern disagree with the observations of Hewitt and Owen (1987). Only the full pipe simulation show the approximate flow pattern like in the experiment. Hence the computing time can only be decreased by a reduction of the pipe length. Therefore only a straight pipe length of 9 m is used in the CFD model, see figure 6.2.

The measure points to calculate the pressure gradient are at the centreline at 7 m and 8 m from the inlet. So that the CFD simulation model have a shorter development length of about 220 diameter than in the experiment.

The mesh consists of parts with hexahedral and tetrahedral cell elements, see figure 6.3.

The outlet box consist of tetrahedral elements. Hexahedral elements can not be used for this section, due to the transition of the pipe to the outlet box.

Due to the rotationally symmetry of the pipe section a 2D mesh can be extruded from a start face to a target face of this section. The extrusion length of one step is 12.2 mm.

The start face is the inlet of the pipe, see figure 6.4. This face consist of 3.5 mm large 2D quadrilateral cell elements.

The 3.5 mm size has been taken from the Fabre mesh study, see section 5.2. The three boundary layers are adjusted, that the wall y^+ value is about 30.

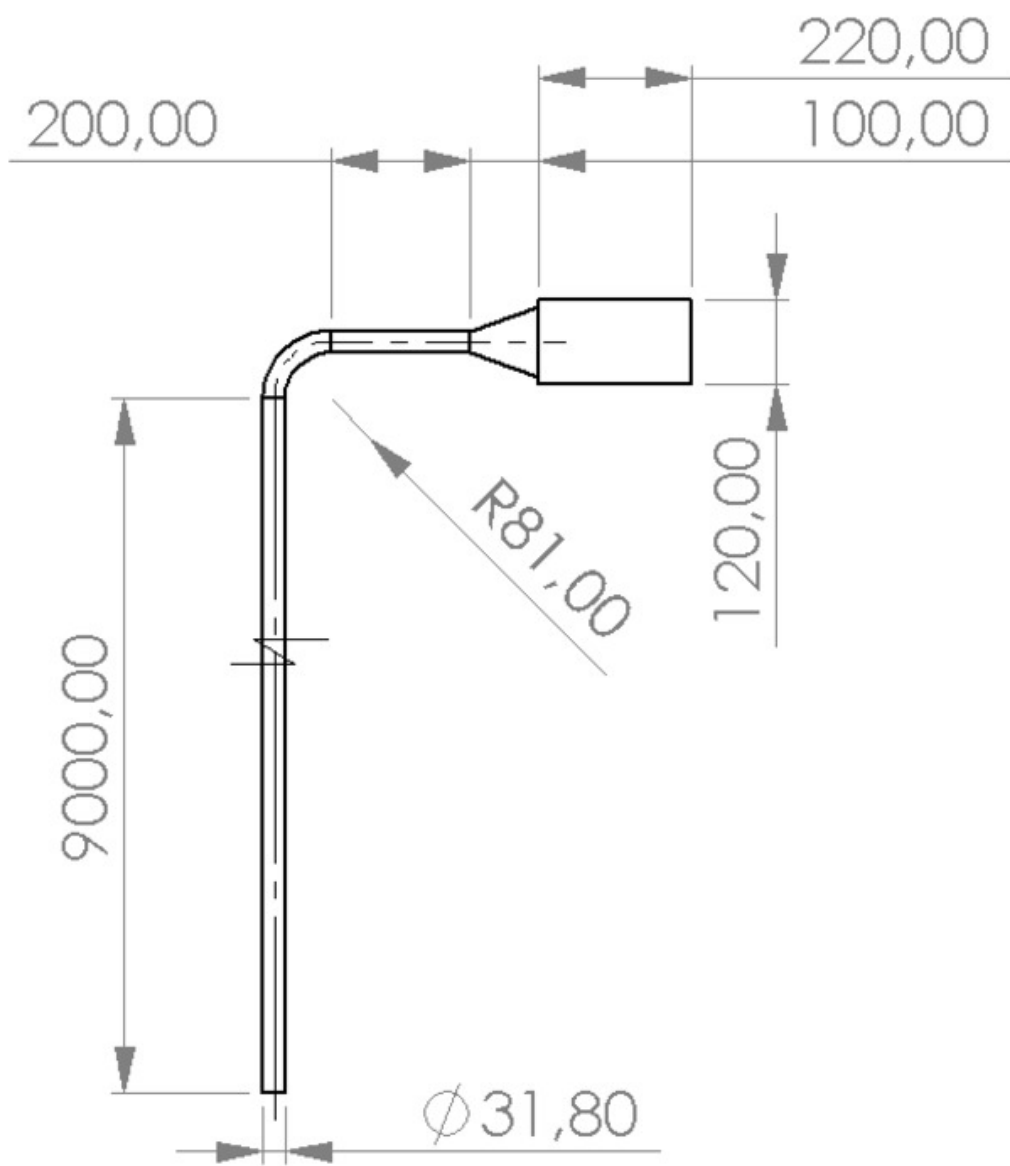


Figure 6.2: Hewitt CFD model drawing with dimensions; figure by the author

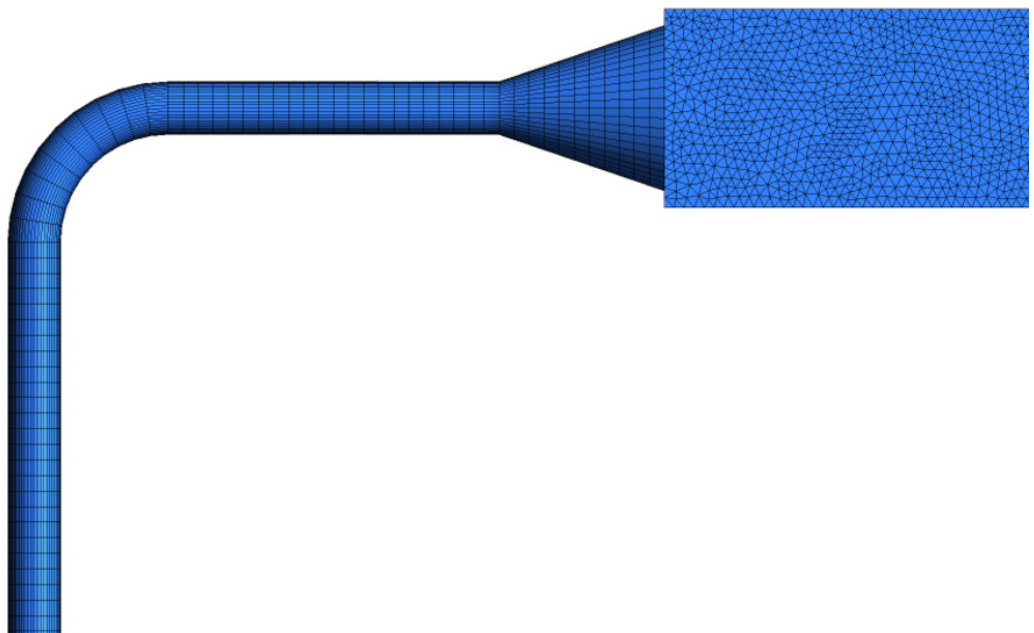


Figure 6.3: Hewitt CFD model; surface mesh; figure by the author

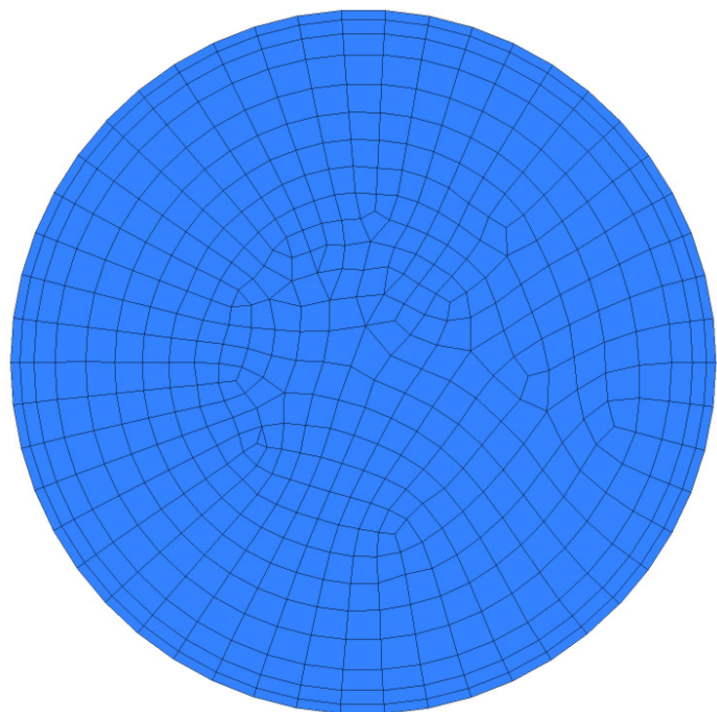


Figure 6.4: Hewitt CFD model; 2D mesh at inlet; figure by the author

6.1.2 Hewitt Boundary Conditions

An overview of the boundary conditions of the CFD model can be seen in figure 6.5.

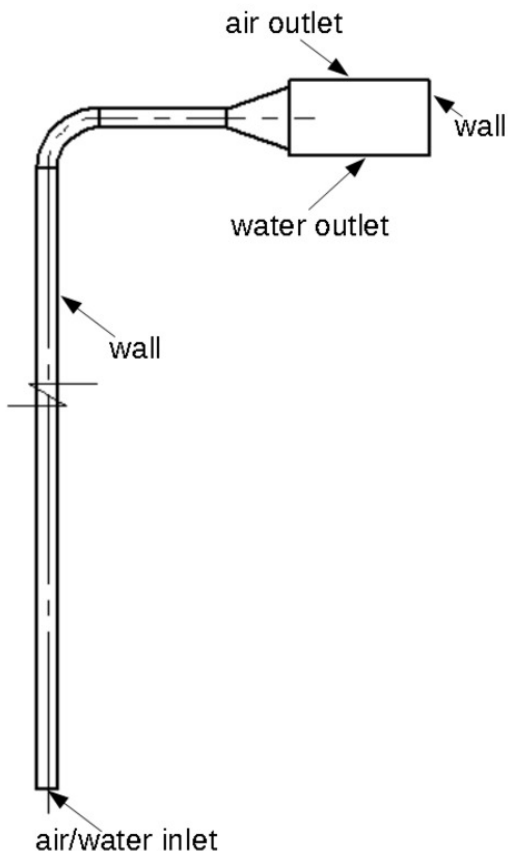


Figure 6.5: Hewitt CFD model; boundary conditions; figure by the author

The inlet condition of this model is changed compared to the experiment. In the CFD it is easier to model a two-phase inlet. Due to this the pipe can be shortened by 2 m, see figure 6.1 and 6.5. The air and water mass flux will be converted with the inlet area to a mass flow. With the corresponding densities the inlet volume fractions can be calculated. The mass flows and the volume fractions are used as input parameter for the inlet boundary condition. The mass fluxes and densities are shown in table 6.1 and 6.2. The air and water outlets are modelled in the same way as the Fabre CFD model, see section 5.1.2. But in this simulation the arbitrary hydrostatic

pressure height is set to 5 mm. Also the wall boundary condition is like in Fabre model, smooth walls with a wall contact angle of 65°.

6.1.3 Hewitt Initial Conditions

The volume fractions on the inlet are calculated in section 6.1.2 and are used for the initial condition. In preliminary simulation it could be seen, that the water hold-up in the pipe is higher than the inlet water fraction. Hence the volume fraction for the water phase is doubled for the initial conditions and the air volume fraction is the difference from the water volume fraction to one. The simulation instability is increased, if the initial air/water mixture is initialised in the outlet box also. Hence the outlet box is initialised only with air.

Because there is water and air inside the pipe, a initial static pressure value is necessary. Due to both phases are homogeneous distributed at the beginning, the mixture density (equation 2.14) can be used to calculate the hydrostatic pressure with the following equation:

$$p_{init} = (\max(y) - y) \ g \ \varrho_{mix} \quad (6.1)$$

The initial velocity upwards is set to the superficial phase velocity, calculated by the corresponding phase volume flow and the pipe cross section area. All other initial velocities are set to zero.

6.2 Vertical Pipe Simulation

Generally it can be said, that the vertical flow simulation has higher demands on the numerical solver. To ensure that the mass and momentum imbalance maximum values are in range of $+/- 1\%$ (see section 5.1.3), the physical timescale have to be set about one magnitude lower than in Fabre horizontal flow simulations. With a physical timescale of 5e-4 s the momentum imbalances in the Hewitt simulations are any time in the specified range. Though due to unsteady flow pattern, the mass imbalances are not balanced but fluctuate with the same curve pattern, see figure 6.6. If these mass imbalance evenly fluctuate around a value and the momentum imbalances are in between $+/- 1\%$, then the simulation can be assumed as converged.

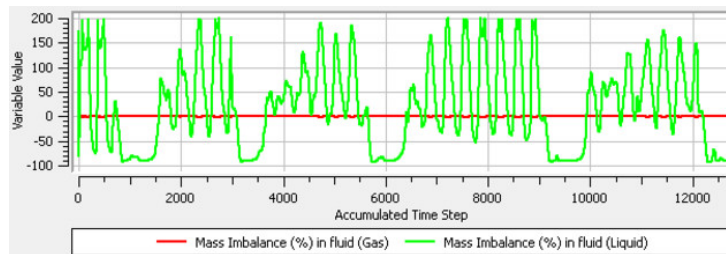


Figure 6.6: Hewitt CFD model, Run No. 6; mass imbalances over iterations; figure by the author

The large deviations higher than 100 % in figure 6.6, is caused by the plug flow. A open boundary condition is used for the outlets and fluid can flow in the computational region, which increase the mass inlet flow.

It can be observed, that the physical timescale did not have only an impact on the simulation stability, also the pressure gradient and the flow pattern depend on the timescale. An increased physical timescale yields to a weaker phase separation, which in turn yields to a decreased water hold-up. With less water content in the pipe, the pressure gradient is decreased and the flow pattern is changed.

A better phase separation, caused by a decreased physical timescale in connection with a parallel run, causes sometimes a floating point exception error,

because of to high gradients. If these high gradients occur at the boundary from one partition to the neighbour partition, the linear solver could become unstable. Hence the advection scheme specific blend factor have to reduce to 0.75, in order to run without a simulation solver error. Though this is tested by 56.000 mesh cells per partition. If this latter value is decreased, it could be that the specific blend factor have to be decreased more.

The results of the CFD simulation can be seen in table 6.3.

Table 6.3: Hewitt proof of concept results; Averaged NPGD, observed flow regime from experiment and CFD simulation

Run No.	NPGD [−]	Flow regime in experiment	Flow regime in CFD simulation
1	0.25	Bubble	Bubble
6	0.13	Plug	Plug

The case FV_190 has a NPGD value of 0.1534. Fortunately the NPGD value for a vertical pipe is close to the horizontal pipe simulation, see table 6.3. Though it can be seen that the NPGD value is increased for a simulation with higher water hold-up. Which could mean that the new CFD simulation model is appropriate to describe flow pattern with larger structures but the NPGD error could increased for flow pattern with small structures like bubble flows or drop flows.

With the shape of the pressure gradient signal, it is possible to derive the flow pattern. The shape of pressure gradient curve of the [Hewitt and Owen \(1987\)](#) CFD simulation, can be seen in figure 6.7.

While the pressure gradient shape of Run No. 1 is roughly sinusoidal shaped, the pressure gradient shape of Run No. 6 is over many iterations constant and followed by a strong increased and decreased pressure gradient in a short period.

The shape of the pressure gradient curve in 6.7 (b) correspond to a plug flow. The pressure gradient curve is constant if no plug reaching the measuring points. If a plug pass the measuring points, the pressure gradient is

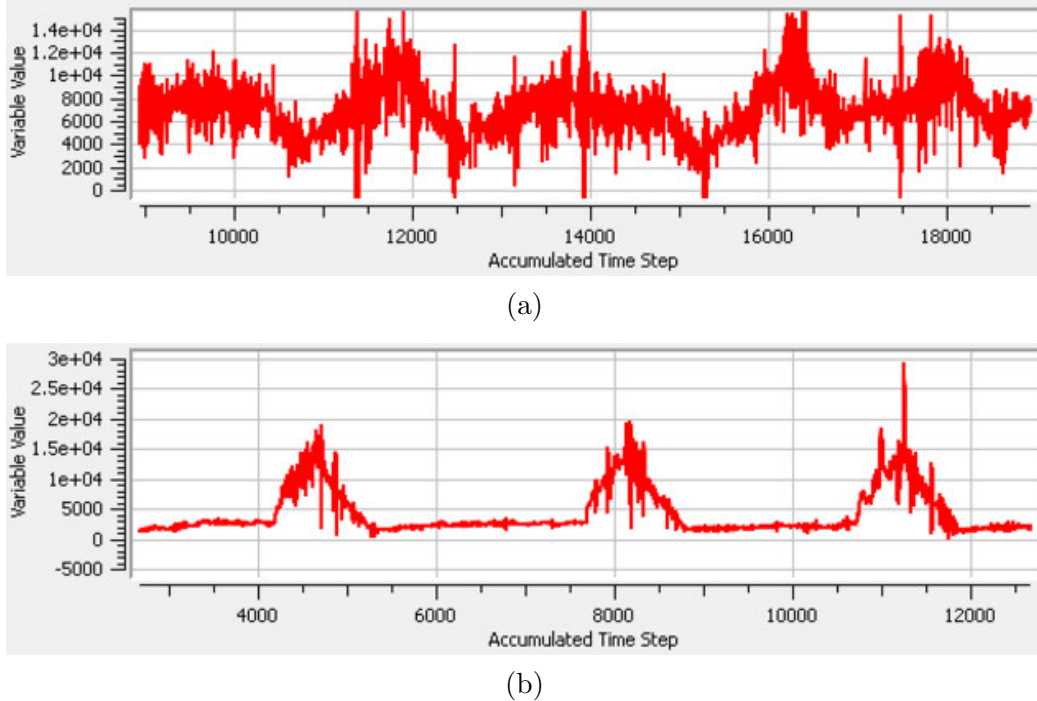


Figure 6.7: Hewitt CFD model pressure gradient over iterations (a) Run No. 1, (b) Run No. 6; figure by the author

increased and decreased. The iterations between two pressure gradient peaks correspond to the distance between two plugs. An example of a plug flow can be seen in figure 2.1 (b). It is assumed, that Hewitt and Owen (1987) called this last mentioned plug flow slug flow, because a plug flow has some large bubbles surrounded by a continuous phase, so that the bubbles are the plugs. In Hewitt Run No. 6 the water hold-up is lower, so that the air is the continuous phase and the water phase will form the plugs like in figure 2.2 (e). Though the slug flow can only occur in horizontal pipes. Hence the author does not follow Hewitt and Owen (1987) by the naming of the above mentioned flow pattern. Hence the notation plug flow is used in this thesis instead of slug flow introduced by Hewitt and Owen (1987), see table 6.3 column "Flow regime in experiment".

In figure 6.7 (a) the pressure gradient shape is between the bubble flow and plug flow. In an ideal bubble flow the bubbles are equally distributed,

that the pressure gradient shape is constant. Described above the pressure gradient shape of a plug flow is constant with pressure gradient peaks in certain distances. A clear signal when a plug reach the measuring point can not be seen in [6.7 \(a\)](#) and therefore it is rather a bubble flow.

The derivative of the flow pattern is carried out by the pressure gradient signal, because it is assumed, that [Hewitt and Owen \(1987\)](#) are used this signal too, to determine the flow pattern. In [Hewitt and Owen \(1987\)](#) there are no comments how they determine the flow pattern, but visual techniques are excluded due to opaque walls in the experiment and special techniques to measure flow pattern like X-ray tomography would have been explained with certainty in the publication.

With the flow pattern derived from the pressure gradient signal, there is a good agreement of the experiment and simulation, see [table 6.3](#). An overview of some simulation results for a exemplary section of the vertical pipe can be seen in the appendix [C](#).

6.3 Hewitt Conclusion

These proof of concept for a vertical pipe flows should examine the generality of the new CFD two-phase model. In order to achieve this, the NPGD values of the vertical pipe simulations have to be equal with the horizontal pipe simulations.

In section 6.2 a good agreement between the vertical pipe and horizontal channel simulation of the pressure gradient error NPGD can be seen. In the vertical pipe simulation, especially for flow pattern with larger structures, the NPGD value is small. For flow pattern with small structures, like a bubble flow, the pressure gradient deviations are increased. On the basis of this knowledge it is assumed, that the force balance in the free surface region is appropriate, but for a dispersed regions further investigations should be carried out. One possible approach to improve the new CFD model is to use a variable SMD correction factor. It could be, that this correction factor of 20 is appropriate for the large interface structures but not for small ones.

The comparison of the flow pattern is not as accurate as the pressure drop, because no description how [Hewitt and Owen \(1987\)](#) determine the flow pattern can be found. And the author can only assumed, that Hewitt used the pressure signal shape to deduce the flow pattern. But overall good agreements can be shown for the flow pattern.

Due to the good agreement of the CFD simulation with the [Hewitt and Owen \(1987\)](#) experiment and comparable error rates with the [Fabre, Masbernat, and Suzanne \(1987\)](#) simulation FV_190, an appropriate two-phase simulation model for horizontal and vertical flow regimes can be assumed. Due to the complexity of this matter, it is recommended to verify this simulation model with other geometries and fluids. Until the new two-phase model is not based on a broader knowledge basis, it is recommended to carry out a validation every time it is used for a new case.

Chapter 7

Proof of Concept with Steam Drum Experiment

Most of all to prevent the carryover of solids into superheaters or turbines have to be guaranteed by the boiler companies, see section 2.2.2. In order to ensure the steam/water separation, there are different separation devices, see section 2.2.3. These separation devices are based often on companies know-how or semi empirical models. Because of the complexity of turbulent two-phase flows in the gravity field, it is very difficult to reproduce such a flow with a numerical model. Epple et al. 2012 For the same reason steam drum experiments are expensive, why only some experiments are carried out and not often published.

To overcome the steam/water separation uncertainty, the overall goal of this thesis is to develop a simulation model to reproduce the droplet flow rates in steam drums. Despite of many two-phase experiments in the literature, no experiment for a steam drum can be found. Hence a steam drum experiment, based on the ERK Eckrohrkessel GmbH design, is carried out.

A schematic drawing off a steam drum with ERK drum internals is shown in figure 7.1.

In this drawing the drum wall with the most important pipe connections, the baffle plates and water levels are shown.

The steam/water mixture arrive the inner of the steam drum through the

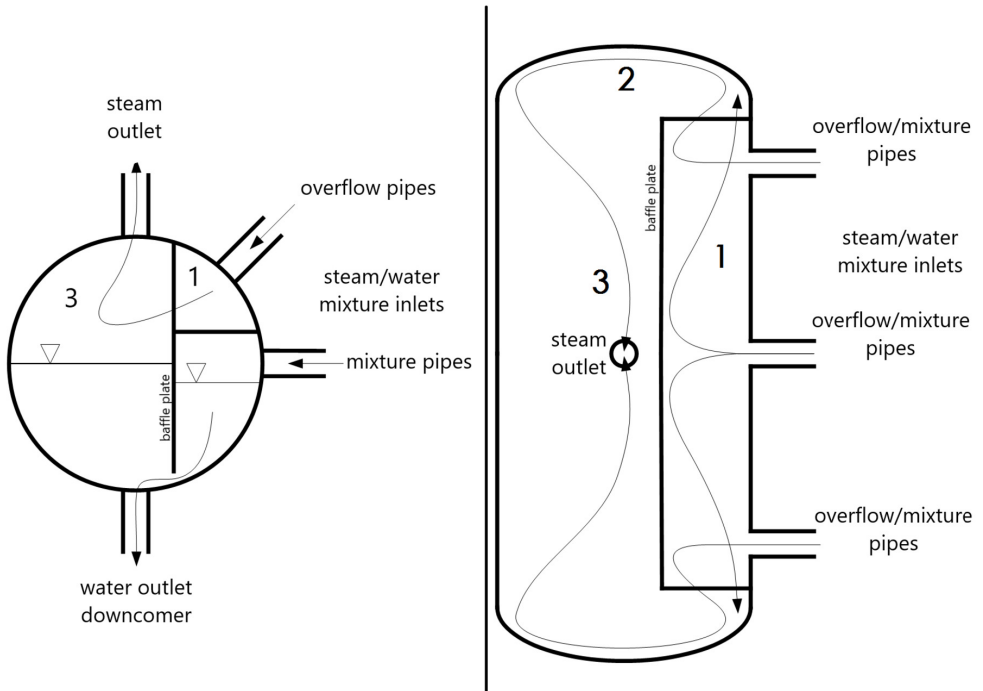


Figure 7.1: ERK steam drum internals schematic drawing; Schreiber, Hellwig, and Nowitzki 2017

overflow and mixture pipes. In the inner of the drum the steam/water separation takes place and water leave the drum through downcomers and the steam through the steam outlet. In order to ensure that the water without bubbles can flow to the downcomers, there is a small opening at the bottom of the baffle plates, that the water can flow underneath. The second opening is the steam window. The steam window is a small open section at the top of the side baffle plates. The steam should only pass the steam window to the steam outlet. The baffle plates delimit the drum inlet region.

Additional the three separation stages are numbered. Stage 1 is nearly enclosed from the drum wall and baffle plates. There the steam/water mixture is separate due to the contact with the baffle plates. A high turbulence increase the contact of the mixture with the walls. Hence region 1 is designed, that the turbulence ensure a good separation and is called “turbulent separation stage”. In separation stage 2, the centrifugal force caused by the redirection at dished heads is used, to push the droplets to the dished head

walls. The separation principle of stage 2 is the same like in a cyclone and is called “centrifugal separation stage” . In stage 3 the velocities have to decreased, in order to separate the steam/water mixture due to the gravity and is called “calm stage” .

The water level position in figure 7.1 is important for the mixture separation too. If is the water level too low, the steam can flow underneath the baffle plate, the separation stage 2 and 3 are not effective and the steam purity is decreased. If is the water level too high, too much water is carried through the steam window and the steam purity is decreased also. Due to always present fluctuations, it is recommended to achieve a half-filled steam drum. Please note that the water level of stage 1 compared to stage 2 and 3 is not the same. Due to the pressure drop of the steam window an increased pressure occurs in stage 1 and pushed down stronger the water level there.

The following CFD simulations of this steam drum experiment should show in a proof of concept, how exact can be a prediction of droplet mass flow out of the turbulent stage. The CFD simulations are based on validation cases FV_170 and FV_190, see section 5.4 and the physics set-up in section 5.1.3. The case FV_200 was neglected, because of unstable behaviour. The complexity of the experiment steam drum simulation is significant increased compared to the Fabre, Masbernat, and Suzanne (1987) and Hewitt and Owen (1987) experiment simulations. Here the CFD model and the physics set-up need a good performance, to limit the computational time to a few hours and ensure a stable run. With an acceptable droplet mass flow prediction and in an acceptable computational time, this simulation set-up should be ready, to be applied to industrial applications.

7.1 Steam Drum Experiment

The steam drum construction and set-up can be seen in Schreiber, Hellwig, and Nowitzki (2017). This experiment is designed for an air/water mixture to determine the droplet mass flow out of the sides, in order to measure the water carry over in the turbulent region in front of the baffle plate (stage 1 in figure 7.1). This experiment steam drum is different to an ERK steam drum, because the carried water droplets from the turbulent inlet region, will be examined only. Hence where in an ERK steam drum a dished head exists, is in the experiment an air outlet. To ensure that all the gas, which pass the steam window, leave the experiment drum at the sides, the rear part (behind the baffle plate) is closed in the experiment drum with extended side baffle plates. Hence the experiment steam outlet has no further task as the pressure regulation only. For comparison ERK steam drums can be seen in figures 2.9 and 2.10.

The experiment steam drum construction is shown in figure 7.2.

The drum wall consist of a polyacrylic pipe, in order to examine the air/water interface and measure the interface position. Two types of inlet pipes exist, mixture and overflow pipes. In both pipes the air/water mixture flow inside the drum, but with different water fraction. Inside the drum the air/water separation takes place, so two types of outlets are needed, one for the water and one for the air. Water is leaving the experiment drum at the three downcomer pipes, whereby the air can leaving the drum at both sides. The baffle plate is to separate the stage 1 from the rest of the steam drum and supports the air/water separation. By this baffle plate, air is forced to flow through the steam windows and the water can only flow through the holes at the bottom of this plate. In order to avoid that air can flow through the baffle plate holes, the water level in this drum have to be higher than the holes, so that the holes are covered with water.

The air/water mass flow ratio, the bulk mass flow, the cross section area of the steam windows as well as the baffle plate position are important parameters for the air flow purity. These parameters are designed by Schreiber, Hellwig, and Nowitzki (2017) for this experiment.

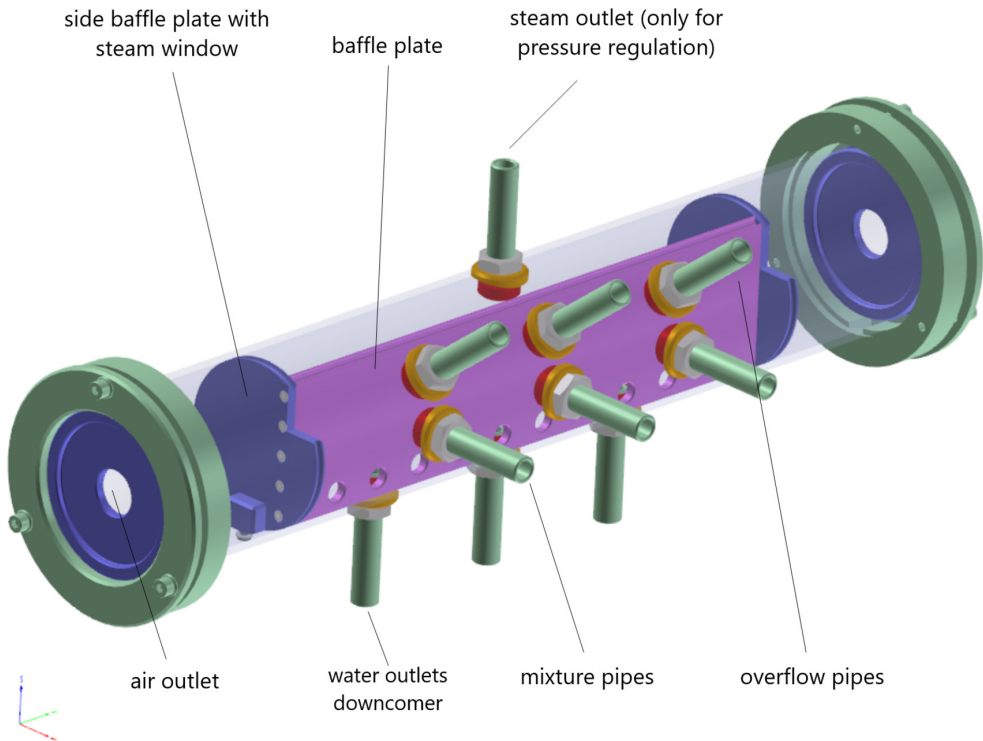


Figure 7.2: Construction of the steam drum experiment; Schreiber, Hellwig, and Nowitzki 2017

To measure the water level height, a marker is stamped on the baffle plate next to the right side baffle plate.

ERK places a pipe network on the top of every boiler, which acts as a pre-separator. This pre-separator pipe network has an effect of the mixture separation inside the steam drum. Hence this pipe network have to be included in the experiment too. How the steam drum and the pre-separator pipes are included in the boiler water circulation is shown in figure 2.5. The experiment pre-separator pipes are shown in figure 7.3.

The three sets of feeding pipes are connected with the three sets of experiment drum inlet pipes. The overflow pipes of the feeding pipes are connected with the overflow inlet pipes on the experiment drum and the mixture pipes respectively. The distributor pipe guide the incoming two-phase mixture to the feeding pipes. Due to the strong mixing in the distributor pipe, it is

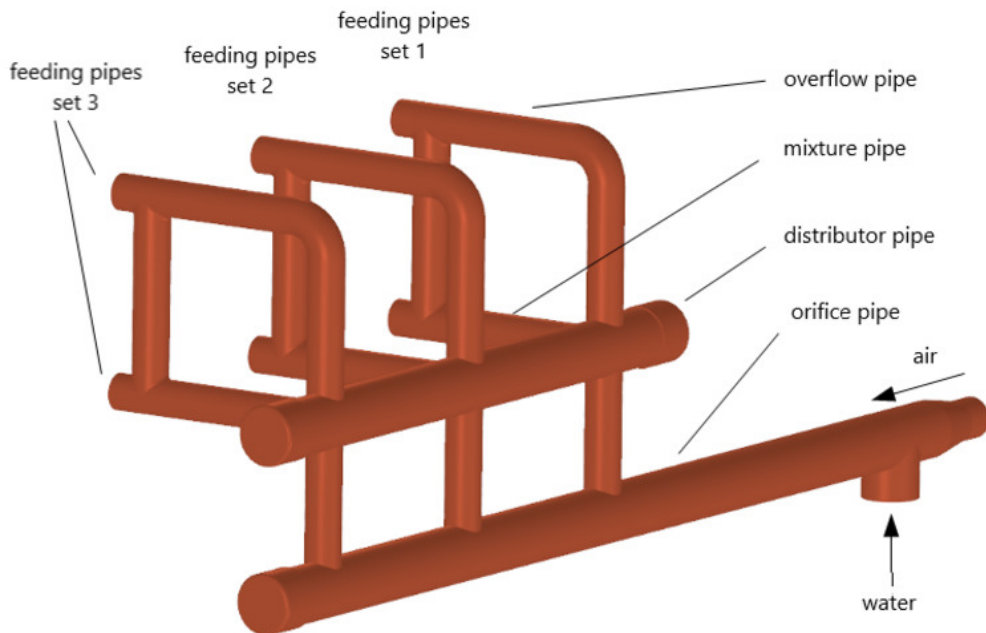


Figure 7.3: Construction of the steam drum experiment feeding pipes; Schreiber, Hellwig, and Nowitzki 2017

assumed that the flow pattern in front of this pipe have only a weak impact of flow pattern in the feeding pipes. Hence it is decided to put the system boundary in front of the distributor pipe.

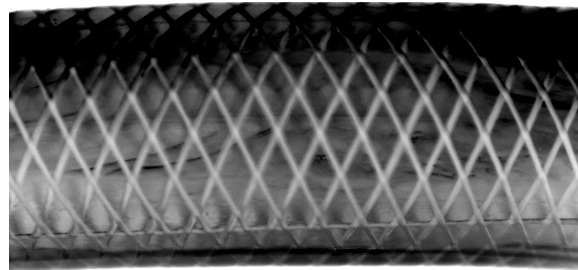
Due to the given conditions an orifice pipe is included in the experiment to feed the distributor pipe with the air/water mixture. The orifice pipe is only a component of the experiment pre-separator. The task of the orifice pipe is to mix the air with the water and supply the mixture equally to the distributor pipe. Hence there are three orifices in the vertical part of the orifice pipe. This is a design error and does not work, because a two-phase mixture can not be equally distributed with this technique. In order to examine the not equally distributed water fraction in the feeding pipes, the connection pipes between the feeding pipes and the steam drum inlets are realised with transparent tubes.

In the experiment feeding pipes it is assumed that a wavy stratified flow and/or a slug flow can occur. These later flow pattern have an unsteady

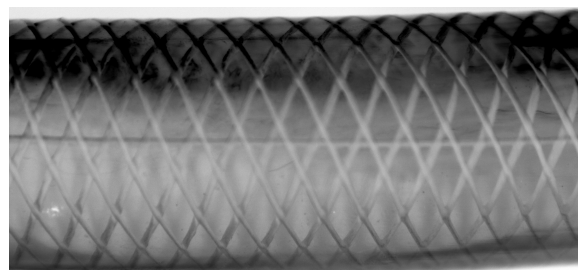
behaviour. Hence to analyse also transient flow pattern, video recordings are carried out. These video recordings showing in every pipe section in set 3 a slug flow regime, but with different water levels and frequencies. A theoretical slug flow can be seen in figure 2.2 (e). But to discuss the water separation in the feeding pipe set 3, only the snapshots in figure 7.4 are needed. The naming of the pipe sections is shown in figure 7.5.

The overflow pipes in sub-figure (c) and (d) have a decreased water level. The air/water mixture is divided partially behind the distributor pipe, so that more water is flowing through the mixture pipe and more air is flowing through the overflow pipe, see figure 7.4 (a) and (c). The following connection pipe between the overflow and mixture pipe cause a further increasing water level in the mixture pipe, see sub-figure (b). Hence the water content of the mixture pipes are higher than in overflow pipes. This different water distribution in overflow and mixture pipe set 3 should be reproduced in the CFD simulation also.

As mentioned above the orifice pipe can not equally distribute the air/water mixture. In Schreiber, Hellwig, and Nowitzki (2017) it can be seen, that in feeding pipes set 3 the water content is much higher than in set 2 and set 2 has a higher water content than in set 1. Those different water levels in the sets cause miscellaneous flow pattern. These miscellaneous flow pattern are a good test for the new CFD model, whether the CFD model can reproduce a wide range of flow pattern.



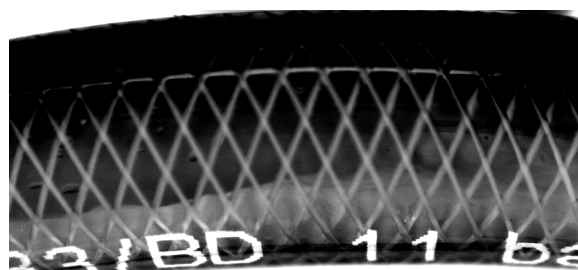
(a)



(b)



(c)



(d)

Figure 7.4: Feeding pipes set 3 visual water level snapshot; case 500 L/h water and 25 m³/h; (a) mixture pipe in front of connection pipe G3.1, (b) mixture pipe behind connection pipe G3.2, (c) overflow pipe in front of connection pipe Ü3.1, (d) overflow pipe behind connection pipe Ü3.2; Schreiber, Hellwig, and Nowitzki 2017

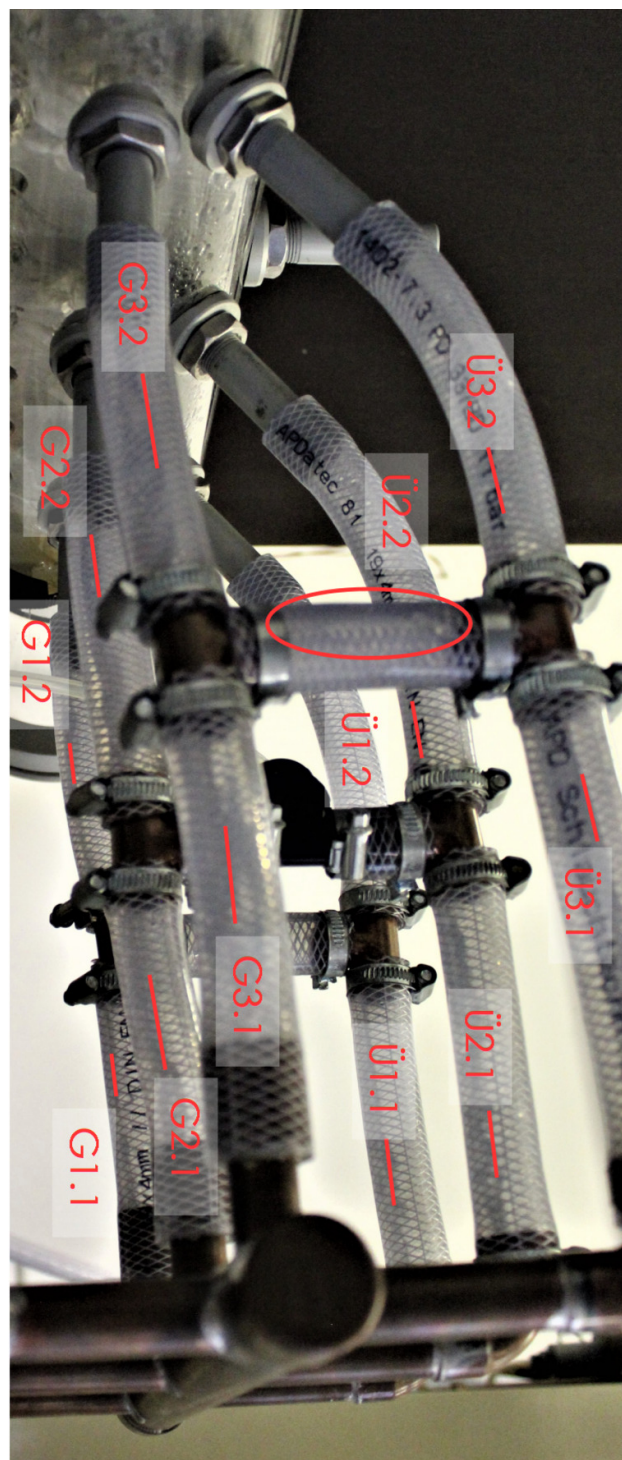


Figure 7.5: Naming of feeding pipes in experiment steam drum regarding water content and flow pattern; Schreiber, Hellwig, and Nowitzki 2017

Due to the transient steam drum inlet behaviour the water interface in stage 1 of the experiment steam drum is unsteady. Because of the flow and water level fluctuation the droplet mass flow fluctuate also. Hence one experiment run should take more than 6 min, in order to overcome this fluctuations. To avoid droplet mass flow deviations due to ambient pressure and temperature changes, the mass flow measurements are repeated on different days. The results of the droplet mass flow at both drum sides is shown in table 7.1.

Table 7.1: Droplet mass flow out of experiment left and right steam drum side

Run	droplet mass flow [kg/s]							
	Day 1		Day 2		Day 3		left	right
	left	right	left	right	left	right		
1	1.35e-05	8.88e-08	1.62e-06	1.06e-06	1.75e-06	3.16e-07		
2	1.16e-05	8.88e-08	1.10e-06	2.83e-07	3.21e-06	2.50e-07		
3	8.21e-06	1.16e-07	4.89e-06	2.61e-07	2.03e-06	1.60e-06		
4	1.05e-05	1.77e-07	4.85e-06	1.72e-07	1.27e-06	3.22e-07		
5	-	-	1.76e-06	4.44e-07	6.72e-07	3.05e-07		
ave	1.09e-05	1.18e-07	2.85e-06	4.44e-07	1.78e-06	5.6e-07		

It is trying to hold the conditions for every run constant. These conditions are the air volume flow of $25 \text{ m}^3/\text{h}$, the water volume flow of 500 L/h and the water level of 21.5 mm below the centreline.

Evident is the difference between the sum of the left side of day 1 in contrast to the others days. It is assumed that at day 1 some discrepancies, regarding the experiment conditions have been occurred, why the measurements at day 1 are discarded. Generally the droplet mass flow out of the right side is smaller than the on the left side. Additional the mass flow fluctuations on the left side are higher than on the right side. That suggests, that on the left side the inlet fluctuations are stronger than on the right side.

7.1.1 Steam Drum CFD Geometry and Mesh

The dimensions of the CFD experiment drum is shown in figure 7.6.

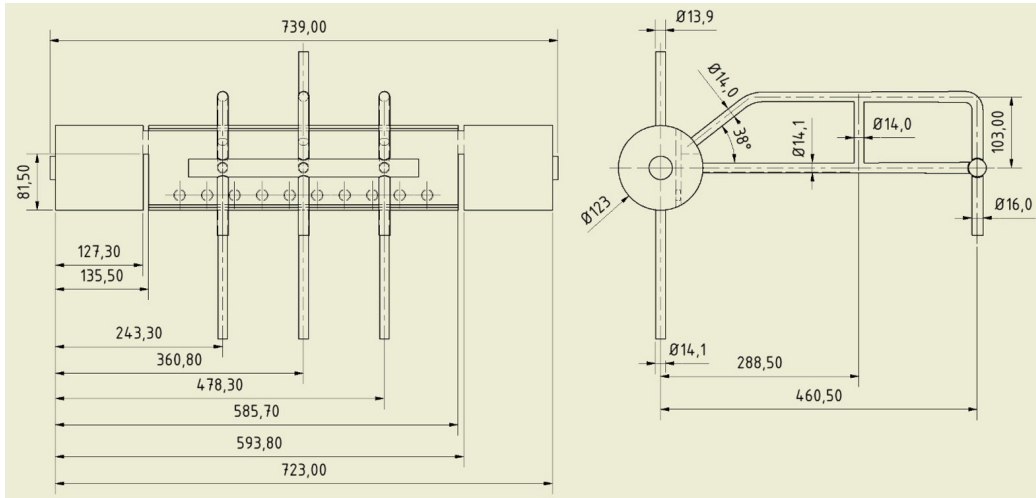


Figure 7.6: CFD Construction of the steam drum experiment with dimensions; Wehner, Hellwig, and Nowitzki 2017

Construction deviations due to production are included in the CFD model, because drum dimensions are determined at the experimental device again and the construction drawing is corrected. The corrected CFD model in 3D can be seen in figure 7.7.

As mesh element type, tetrahedral cells are used. This type provide a fast meshing for complex geometries. Therefore this type is used often in industrial applications. Though the tetrahedral cells have disadvantages by the numerical error in contrast to the hexahedral cell type. To reduce the numerical error a finer mesh of tetrahedral mesh is recommended compared to a hexahedral mesh. Hence global mesh parameters are used for the base mesh, with local refinements. The global mesh parameters for the mesh program "CFX Mesh" can be seen in table 7.2.

Table 7.2: Steam drum experiment global mesh parameters

Size Function	Proximity and Curvature
Min Size	0.3 mm
Proximity Min Size	0.3 mm
Max Face Size	30.0 mm
Max Tet Size	60.0 mm

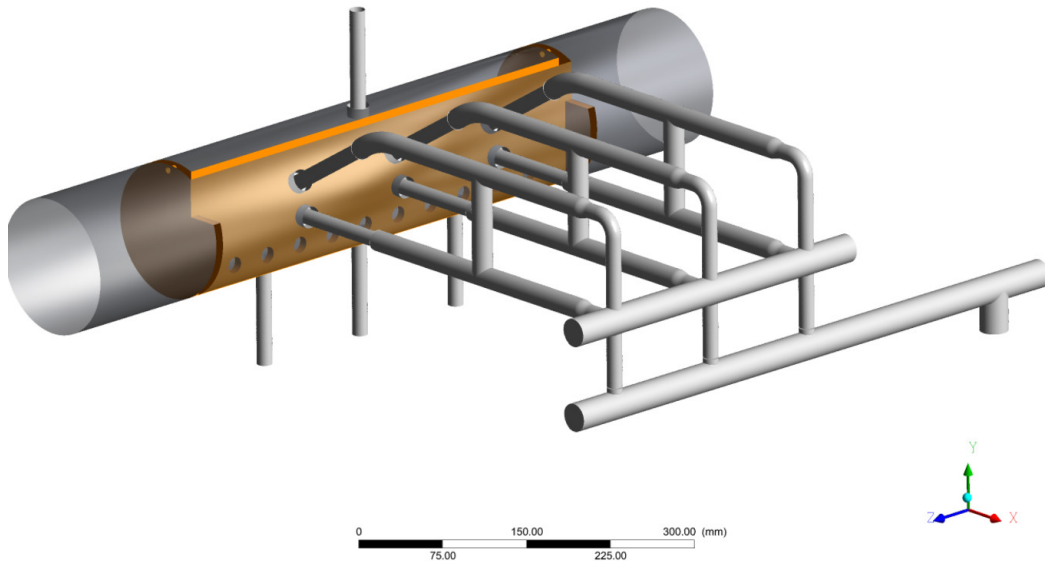


Figure 7.7: 3D drawing of the experiment steam drum; figure by the author

The local refinements are placed at neuralgic positions. At neuralgic positions large gradients of velocities or volume fraction are assumed, who a coarse mesh can cause solver instabilities or are crucial for the accuracy. An overview of the neuralgic positions and the local refinement value is shown in table 7.3.

Table 7.3: Steam drum experiment local refinement mesh parameters

Steam Drum Two-Phase Interface	3.0 mm
Feeding Pipes Wall Surface	1.0 mm
Inner Drum Pipes Surface	1.0 mm
Orifices Edges	0.2 mm
Baffle Plates Surfaces	5.0 mm
Steam Drum Wall Surface	3.0 mm

At steam drum two-phase interface, in the feeding pipes, at the baffle plates and at the steam drum wall especially large volume fraction gradients are assumed. Large velocity gradients are assumed at inner drum pipes (stuck-

through nozzles) and at the orifices.

An overview of the mesh on a cutting plane can be seen in figure 7.8.

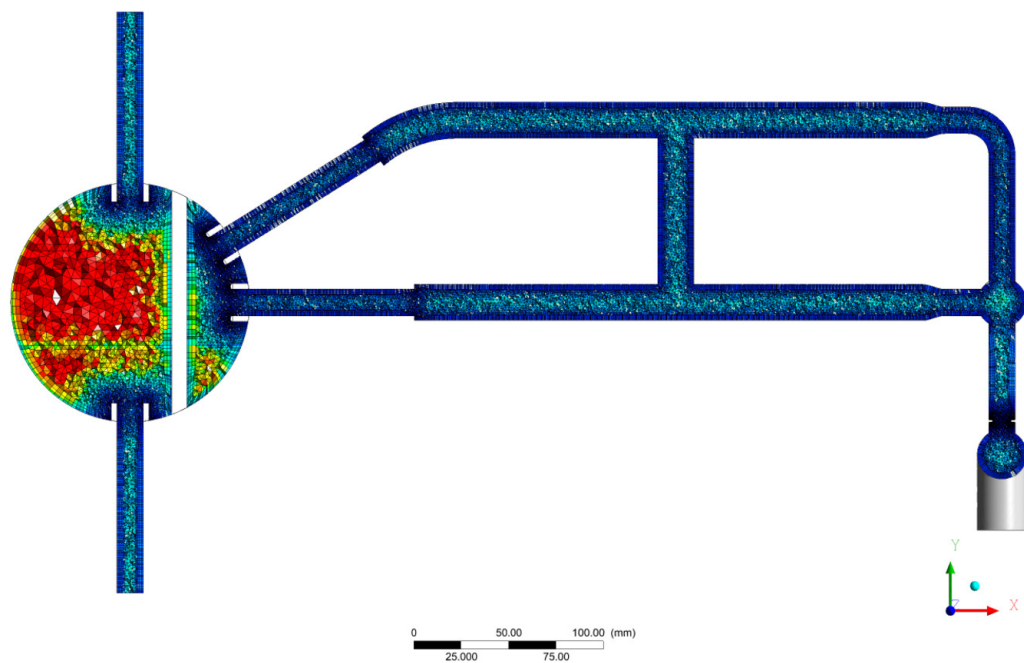


Figure 7.8: Mesh overview of the experiment steam drum cut; Coloured by volume size; figure by the author

For mesh details one can see figure 7.9.

Larger figures of sub-figures in 7.9 can be found in the appendix D.1 - D.4.